AGU PUBLICATIONS

JGR

Journal of Geophysical Research: Atmospheres

RESEARCH ARTICLE
10.1002/2013JD020855

Key Points:
- The developed algorithm is simple, fast, and sensitive to the presence of dust
- Can capture both the outbreak and transport of dust event very well
- Detections are found to be accurate at 70% over land and 82% over ocean

Correspondence to:
P. Ciren,
pubu.ciren@noaa.gov

Citation:
Ciren, P., and S. Kondragunta (2014), Dust aerosol index (DAI) algorithm for MODIS, *J. Geophys. Res. Atmos.*, *119*, 4770–4792, doi:10.1002/2013JD020855.

Received 9 SEP 2013
Accepted 19 MAR 2014
Accepted article online 23 MAR 2014
Published online 24 APR 2014

Dust aerosol index (DAI) algorithm for MODIS

Pubu Ciren[1,2] and Shobha Kondragunta[2]

[1]I.M. Systems Group Inc., Rockville, Maryland, USA, [2]NOAA/NESDIS Center for Satellite Applications and Research, College Park, Maryland, USA

Abstract A dust aerosol index (DAI) algorithm based on measurements in deep blue (412 nm), blue (440 nm), and shortwave IR (2130 nm) wavelengths using Moderate Resolution Imaging Spectroradiometer (MODIS) observations has been developed. Contrary to some dust detection algorithms that use measurements at thermal IR bands, this algorithm takes advantage of the spectral dependence of Rayleigh scattering, surface reflectance, and dust absorption to detect airborne dust. The DAI images generated by this algorithm agree qualitatively with the location and extent of dust observed in MODIS true color images. Quantitatively, the dust index generated for hundreds of dust outbreaks observed between 2006 and 2013 were compared to Cloud Aerosol Lidar with Orthogonal Polarization (CALIOP) Vertical Feature Mask (VFM) product and the detections are found to be accurate at 70% over land and 82% over ocean. The Probability of Correct Detection (POCD) is 80% over land and 76% over ocean. The dust detections with DAI-based dust identification algorithm were also compared to 5 years of Aerosol Robotic Network (AERONET) observations for 13 stations with a wide range of geographical coverage. The average detection accuracy is ~70%, whereas the POCD is ~67%. The performance of DAI-based dust detection against AERONET is slightly weaker than that against CALIOP VFM because of the limited number of matchups for some stations. For stations close to source region or coastal and island stations, the accuracy and POCD can be as high as ~85% and ~89%, respectively.

1. Introduction

Dust influences weather and climate, air quality, hydrological cycle, and ecosystems [*Nicholson*, 2000; *Prospero and Lamb*, 2003; *Yoshioka and Mahowald*, 2007; *Kim et al.*, 2010; *Al-Saadi et al.*, 2005; *Zhao et al.*, 2011; *Tan et al.*, 2011]. It perturbs the Earth's radiation budget, directly by scattering and absorbing solar radiation, by affecting the transfer of the terrestrial thermal emission, and indirectly by altering cloud properties and lifetimes. To understand these effects, monitoring its global distribution routinely including sources and transport is crucial [*Intergovernmental Panel on Climate Change*, 2007]. Remote sensing from space provides an unprecedented capability to monitor the spatial and temporal variability of dust.

Due to its optical properties, dust exhibits distinct radiative signatures in the UV, visible, and IR regions [*Sokolik*, 2002]. Various satellite-based dust detection techniques have been developed by utilizing its signature either in the UV [*Herman et al.*, 1997], visible [*Miller*, 2003; *Jankowiak and Tanré*, 1992; *Martins et al.*, 2002; *Kaufman et al.*, 1997], IR [*Ackerman*, 1997; *Darmenov and Sokolik*, 2005; *Hansell et al.*, 2007], or a combination of visible and IR [*Evan et al.*, 2006; *Xie*, 2009; *Zhao et al.*, 2010; *Cho et al.*, 2013]. Strong absorption by dust and low-surface reflectivity in the UV spectral region enables the detection of absorbing aerosol including dust in the atmosphere [*Herman et al.*, 1997]. In addition, unlike most other dust detection techniques which can only provide a simple binary mask, absorbing aerosol index (AI) is also associated with the intensity of dust, although quantifying the dust loading in terms of optical depth requires the knowledge of dust layer height [*Hsu et al.*, 1999; *Torres et al.*, 2002]. However, UV aerosol detection technique is limited by its inability to separate dust from other absorbing aerosol such as smoke. Dust absorption features in the visible region (a brownish color as seen by human eyes) is well utilized to detect dust using spectral and spatial variability tests [*Miller*, 2003; *Darmenov and Sokolik*, 2009; *Zhao et al.*, 2010; *Cho et al.*, 2013]. However, clouds, other type of aerosols, and bright surfaces can become a major interference. A unique radiative signature of dust in the IR window region, i.e., a negative brightness temperature difference between 11 μm and 12 μm, is widely used to distinguish the effect of dust from that of clouds [*Sokolik*, 2002; *Legrand et al.*, 2001; *Bullard et al.*, 2008]. Some algorithms use 8.5 μm in addition to 10 μm and 11 μm to detect dust using tri-spectral differencing techniques [*Hu et al.*, 2008; *Ackerman*, 1989, 1997; *Ashpole and Washington*, 2012]. However, as *Darmenov and Sokolik* [2005] indicated that the magnitude or even the sign of the brightness temperature difference depends on the composition of the dust, height of the dust

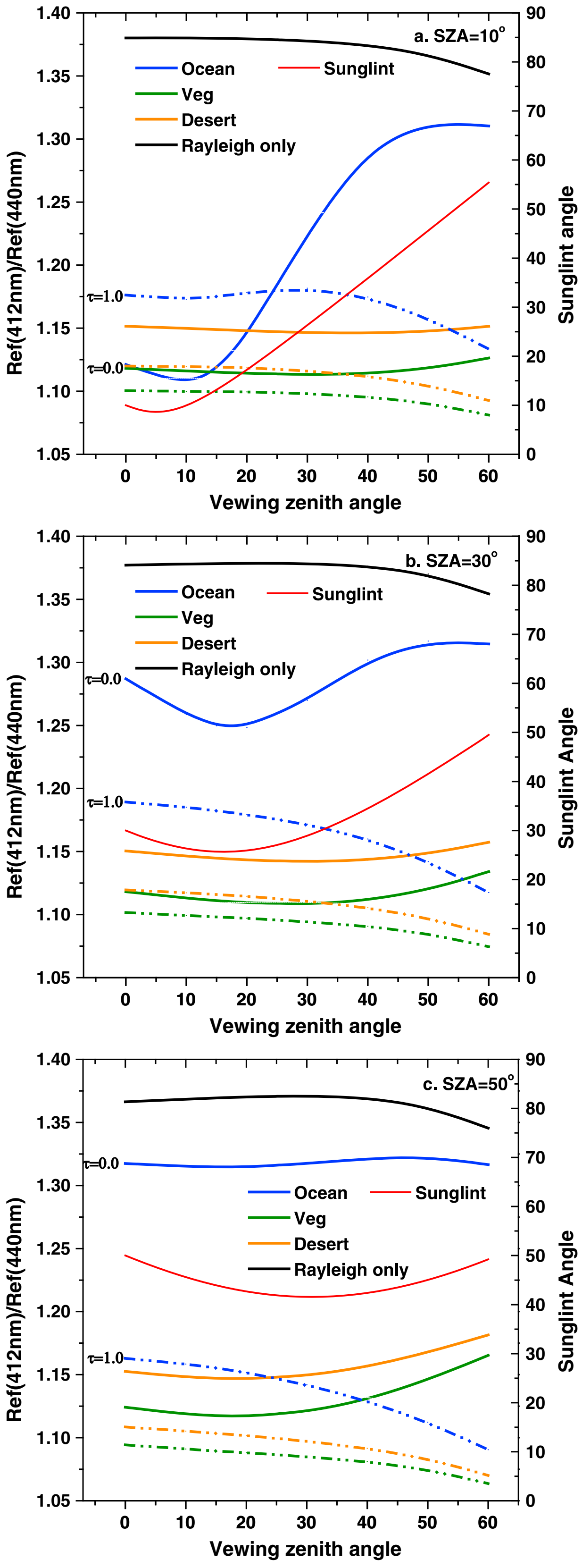

Figure 1

layer, and surface emissivity, and thus, the ability of detecting dust can vary from location to location. In addition, another complication with IR detection of dust is from the water vapor absorption in longwave IR, which significantly affects the detection over regions and/or seasons depending on atmospheric water vapor content [*Ashpole and Washington*, 2012]. Besides utilizing the dust signature in brightness temperature difference between 11 μm and 12 μm, *Klüser and Schepanski* [2009] further utilized the dust effect on diurnal cycle of brightness temperature in 11 μm to derive a bitemporal mineral dust index for Meteosat Second Generation IR observations. However, it is only for over land, applicable only to geostationary satellite observations, and based on the assumption, that diurnal variability of dust plume is small, which is not always true for transported dust.

Besides separating clouds from other type of aerosols, the challenge of detecting dust lies largely in separating it from a bright surface that is generally the source of airborne dust. In the deep blue to blue wavelength region, reflectance from a bright surface is well below the critical surface reflectance: a quantity to define if signal from aerosol is distinguishable from the surface. A deep blue aerosol optical depth algorithm developed by *Hsu et al*. [2004] shows aerosol properties can successfully be retrieved even over a bright surface, when measurements at deep blue channels are used. In the deep blue aerosol retrieval algorithm, deep blue aerosol index (AI) defined in a manner similar to the Total Ozone Mapping Spectrometer (TOMS) AI is used for cloud screening to separate aerosol from clouds but aerosol type is determined using the aerosol model selected in the aerosol optical thickness retrieval

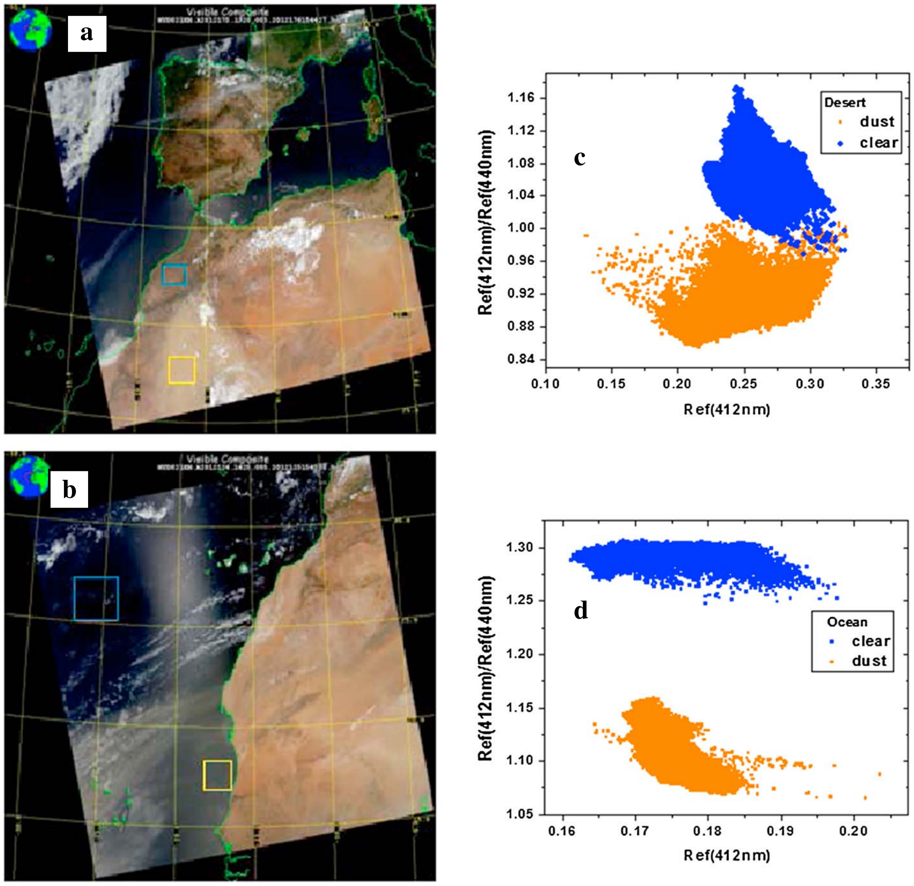

Figure 2. (a) RGB composite image of MODIS Aqua Granule on 3 May 2012, 1425 UTC; (b) RGB composite image of MODIS Aqua granule on 23 June 2012, 1320 UTC; ratio of the observed TOA reflectance at MODIS band 8 (412 nm) and band 9 (440 nm) as a function of the observed TOA reflectance at MODIS band 8 (412 nm) for pixels identified as clear (blue) and dust-laden (orange) (c) over land and (d) over ocean.

algorithm. Note that, like TOMS AI, the AI described by *Hsu et al*. [2004] cannot separate dust from other absorbing aerosols.

A simple and fast dust detection algorithm based on observations in the deep blue (412 nm), blue (440 nm), and shortwave IR (2130 nm) bands which utilizes the spectral dependence of dust absorption, surface reflectance, and differences in absorbing/scattering properties between small and large particles has been developed. This paper describes the theory, test procedure of the algorithm using Moderate Resolution Imaging Spectroradiometer (MODIS) radiances, and evaluation of the DAI-based dust identification algorithm using Cloud-Aerosol Lidar with Orthogonal Polarization (CALIOP) Vertical Feature Mask (VFM) and Aerosol Robotic Network (AERONET) observations.

2. Aerosol Index for Dust and Nondust

The advantage of using measurements in the blue wavelength region (410 to 490 nm) to retrieve aerosol optical properties has been clearly demonstrated by *Hsu et al*. [2004, 2006]. Due to the fact that the sensitivity of reflectance to the dust in the atmosphere decreases with the increasing wavelength, the spectral contrast

Figure 1. Ratio of the simulated TOA reflectance at MODIS band 8 (412 nm) and band 9 (440 nm) as a function of viewing zenith angle at a solar zenith angle of (a) 10°, (b) 30°, and (c) 50°. Solid lines represent a clear atmosphere bounded by ocean (blue), vegetation (green), and desert (orange). Dashed lines represent an atmosphere with dust (AOD at 550 nm is 1.0) bounded by ocean (blue), vegetation (green), and desert (orange). Red solid lines are sunglint angle over ocean. Relative azimuth angle of 120° is used. Total ozone amount is set at 350 Dobson unit (DU).

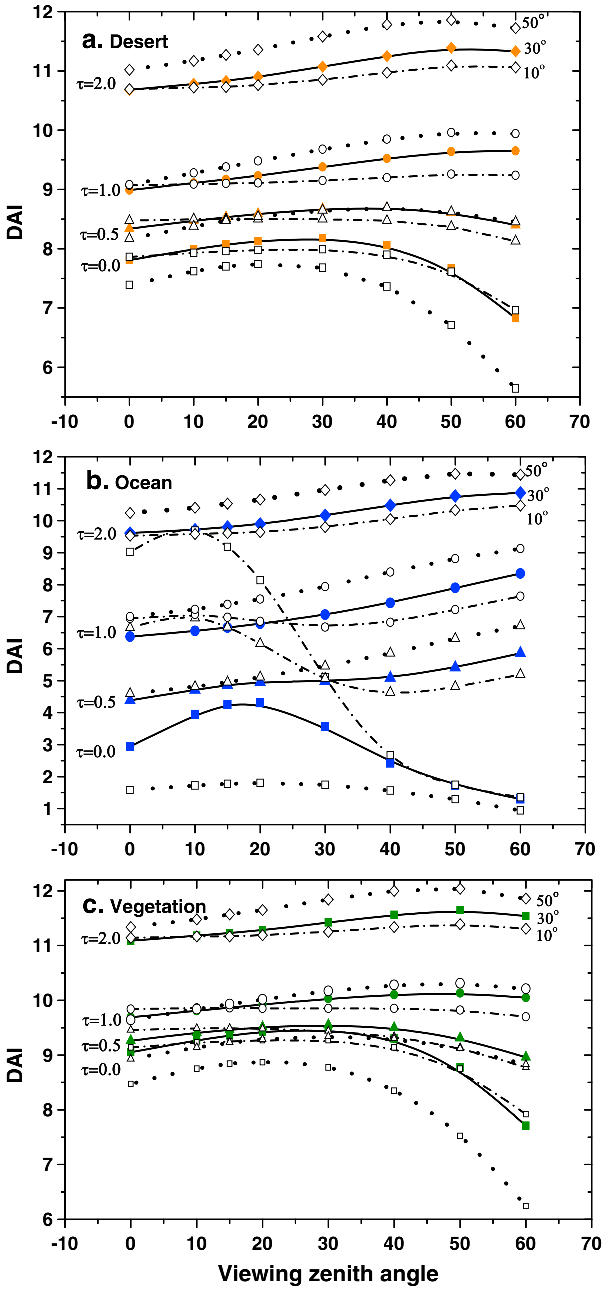

Figure 3. DAI as a function of viewing zenith angle (a) over desert, (b) over ocean, and (c) over vegetation, for aerosol optical depth at 550 nm (τ) of 0.0 (square), 0.5 (triangle), 1.0 (circle), and 2.0 (diamond). Solar zenith angle (SZA) of 10°, 30°, and 50° is represented by dash-dotted, solid, and dotted lines, respectively. Note that relative azimuth is set at 120°.

between two neighboring wavelengths can be used as an indicator for the presence of dust. The spectral shape of the reflectance at the Top of the Atmosphere (TOA) for a cloud-free atmosphere is determined by three main processes: Rayleigh scattering, absorption and scattering by aerosols, and reflection by the underlying surface. The strong wavelength-dependent Rayleigh scattering creates a strong contrast between two neighboring wavelengths. The presence of dust, however, reduces this contrast as a result of the increased absorption with decreasing wavelength. As for the underlying surfaces, their effects on spectral contrast depend on the spectral variability of surface reflectance. For surface type such as water, the surface reflectance is nearly independent of wavelength within deep blue to blue region except for areas with sunglint; therefore, its effect on the spectral contrast is minimal. However, arid or desert surfaces show an increased reflection with the increasing wavelength [*Hsu et al.*, 2004], similar to absorbing aerosol; reflection from these surfaces will also reduce the spectral contrast.

This is illustrated by simulating the spectral dependence of TOA in the blue wavelength region for different surface and atmospheric conditions with a thoroughly tested vector version of 6S radiative transfer code [*Kotchenova et al.*, 2006]. Figure 1 shows the ratio between MODIS band 8 (412 nm) and band 9 (440 nm) TOA reflectance at three solar zenith angles (SZA) (i.e., 10°, 30°, and 50°) for various scenarios: (a) an atmosphere with only Rayleigh scattering bounded by a black surface (surface reflectance of 0.0), (b) an atmosphere with Rayleigh scattering bounded by desert, vegetation and water, and (c) an atmosphere with Rayleigh scattering and dust bounded by desert, vegetation, and water. Note that, the sunglint angles are also shown to illustrate the sunglint region over ocean.

In Figure 1, for different scenarios, dashed line and solid lines represent dust-free and dust with an aerosol optical depth (τ) of 1.0, respectively. A nonspherical dust, i.e., spheroid dust model, based on almucantur inversion of AERONET observations [*Dubovik et al.*, 2006] is used in the simulations. The details of the microphysical/optical

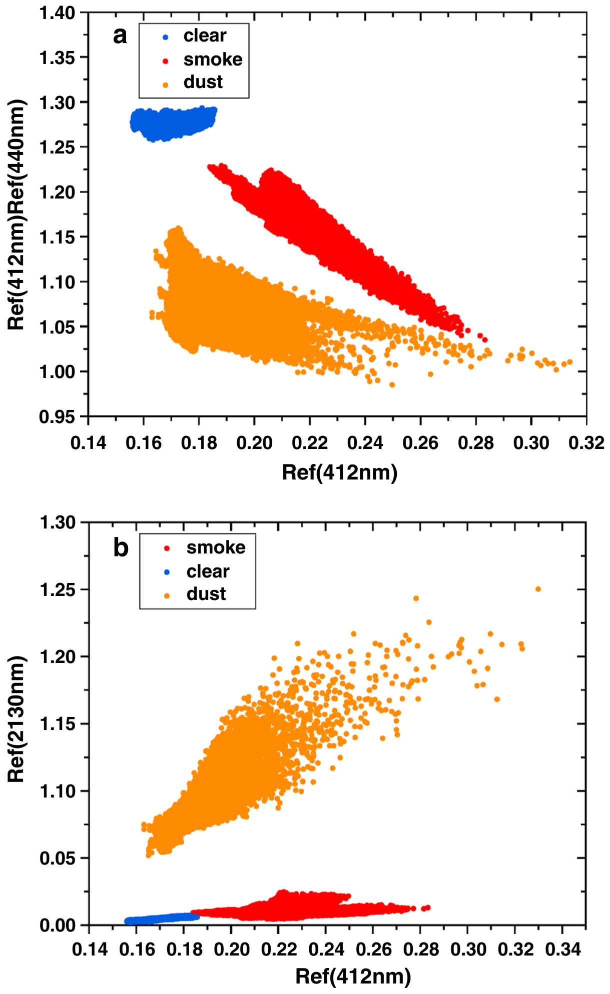

Figure 4. Ratio of the observed TOA reflectance at (a) MODIS band 8 (412 nm) and band 9 (440 nm), and (b) MODIS band 8 (412 nm) and band 7 (2130 nm), as a function of the observed TOA reflectance at MODIS band 8 (412 nm) for pixels identified as clear (blue), smoke-laden (red), and dust-laden (orange) over ocean.

properties of the dust model were given by *Remer et al*. [2006]. Surface spectral reflectance of vegetation and sand embedded in 6S are used to represent vegetated and desert surface. Ocean bidirectional reflectance distribution function from 6S was selected to calculate the ocean surface reflectance for an easterly wind speed of 6 m/s. It is seen that the contrast between reflectances at 412 nm and 440 nm become smaller when dust is present in the atmosphere for desert, vegetation, and sunglint-free (with a sunglint angle > 30°) ocean surface, compared to dust-free condition. The reduction in contrast between the two wavelengths is most significant for sunglint-free ocean surface and relatively smaller for desert and vegetated surfaces because sunglint-free ocean surface has a relatively lower and flat spectral reflectance. For a clear atmosphere over ocean outside of sunglint region, TOA reflectance is dominated by the spectral signature of Rayleigh scattering. While desert and vegetated surfaces are brighter and have spectrally increasing reflectance that is opposite to the spectral signature of Rayleigh scattering. Therefore, the spectral variation of TOA reflectance is reduced for dust-free atmosphere over desert and vegetation. In addition, it is also seen that the decrease in spectral contrast is larger at both a larger viewing zenith angle (VZA) and a larger SZA, since the slant path increases with the increasing SZA and VZA. However, it is also seen that the spectral contrast decreases largely with the decreasing sunglint angle for ocean surface without dust, indicating that reflection from sunglint itself may reduce the spectral contrast as well. This has to be taken into account to avoid misidentifying sunglint as dust.

The reduction in spectral contrast of Rayleigh scattering when dust is present in the atmosphere is also seen in satellite observations. Figures 2a and 2b show the boxes where pixels are identified as clear and as dusty, respectively for over land and ocean. Figures 2c and 2d shows the ratio of TOA reflectance at 412 nm and 440 nm as a function of TOA reflectance at 412 nm for pixels from the selected boxes over land and over ocean. It is seen that the ratio of 412 nm to 440 nm for pixels with dust is distinct from clear pixels over ocean, showing the reduced contrast between 412 nm and 440 nm (see Figure 2d). Such separation is also seen for dust over desert (Figure 2c), although not as distinct as that for over ocean.

This analysis based on theory and observations suggests that the effect of dust in reducing the spectral contrast between 412 nm and 440 nm could be used as a way to detect the presence of dust in the atmosphere. However, using the spectral contrast under clear condition as a reference to detect dust

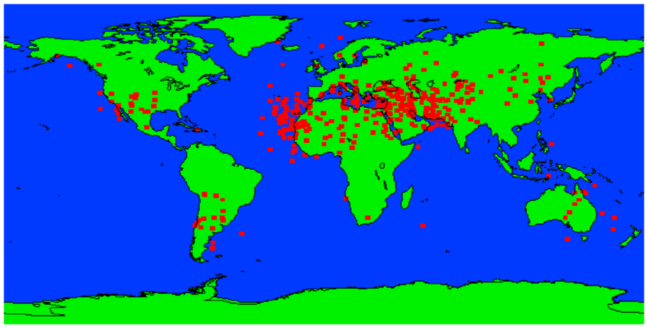

Figure 5. Locations of MODIS Aqua granules used to derive DAI and NDAI thresholds.

requires the knowledge of spectral reflectance of underlying surface. To bypass this problem, the spectral contrast from a pure Rayleigh scattering is used as a reference, and different thresholds for the reduction in spectral contrast is chosen for different surface types. Therefore, an index similar to AI and absorbing aerosol index used in Sea-viewing Wide Field-of-view Sensor [*Hsu et al.*, 2000], named as dust aerosol index (DAI) shown in equation (1) has been developed.

$$\mathrm{DAI} = -100\left[\log_{10}\left(R_{412\mathrm{nm}}/R_{440\mathrm{nm}}\right) - \log_{10}\left(R'_{412\mathrm{nm}}/R'_{440\mathrm{nm}}\right)\right] \tag{1}$$

In equation (1), R is the TOA reflectance and R' is the reflectance from Rayleigh scattering as computed by 6S code for a given location and satellite viewing geometry. To illustrate how DAI changes with the dust loading, 6S radiative transfer model simulations were used to calculate DAI for dust with different optical depths (at 550 nm): no dust ($\tau = 0.0$), weak ($\tau = 0.5$), heavy ($\tau = 1.0$), and extreme dust loading ($\tau = 2.0$). Results are given in Figures 3a–3c, showing the DAI as a function of viewing zenith angle, respectively for over desert, over ocean, and over vegetation. Filled square, triangle, circle, and diamond respectively represent different dust loading indicated by dust aerosol optical depth at 550 nm (τ) of 0.0, 0.5, 1.0, and 2.0. Dash-dotted, solid, and dotted lines are for solar zenith angles of 10°, 30°, and 50°, respectively. The DAI values for heavy and extreme dust loadings are well separated from those of no dust for both desert and vegetation surface and especially for ocean surface outside sunglint region, indicating DAI is well suitable to detect heavy to extreme dust over both land and ocean. For over desert and vegetation, it is clearly seen that the separation increases with the increasing solar zenith angle and the increasing viewing zenith angle, suggesting DAI performs better for a larger solar and viewing zenith angle. And, the difference in DAI becomes smaller with the increasing dust loading. However, it should also be noted that the DAI threshold to detect dust has to be carefully chosen to minimize false alarms and maximize detection, especially for low aerosol loading at a lower solar and viewing zenith angle. Over ocean, it is seen that sunglint is a large factor to cause weak dust not detectable over sunglint region. As for over sunglint-free ocean, the separation between weak dust (represented by $\tau = 0.5$) and no dust (represented by $\tau = 0.0$) is much larger than those over land surface and is less sensitive to the changing solar and viewing zenith angles. This finding suggests that detecting low to weak dust with DAI is much better over ocean than over land surface.

Other absorbing aerosol such as smoke also shows a similar effect on the spectral contrast between 412 nm and 440 nm as dust (Figure 4a). Therefore, using DAI alone can lead to misidentification of smoke as dust. To prevent this, a second index, named as nondust absorbing aerosol index (NDAI) is computed using the formula shown in equation (2).

$$\mathrm{NDAI} = -10\left[\log_{10}\left(R_{412\mathrm{nm}}/R_{2130\mathrm{nm}}\right)\right] \tag{2}$$

Table 1. Criteria Used to Determine Dust and No-Dust Pixels Over Both Land and Water, and Smoke and No-Smoke Pixels Over Both Land and Water

	Dust		Smoke	
	Present	Absent	Present	Absent
Land	$\mathrm{AOD}^a > 0.$ $\mathrm{AE}^a < 0.5$	$0.0 < \mathrm{AOD}^a < 0.2$ $\mathrm{AE}^a \geq 1.0$	$\mathrm{AOD} > 0.5$ $\mathrm{AE} > 1.0$	$0.0 < \mathrm{AOD} < 0.2$
water	$\mathrm{AOD} > 0.5$ $\mathrm{AE} < 0.9$ $\mathrm{FMW} < 0.3$	$0.0 < \mathrm{AOD} < 0.2$ $\mathrm{FMW} > 0.7$	$\mathrm{AOD} > 0.5$ $\mathrm{AE} \geq 1.0$ $\mathrm{FMW} > 0.7$	$0.0 < \mathrm{AOD} < 0.2$ $\mathrm{FMW} < 0.3$

[a] Represents AOD and AE from MODIS deep blue retrievals.

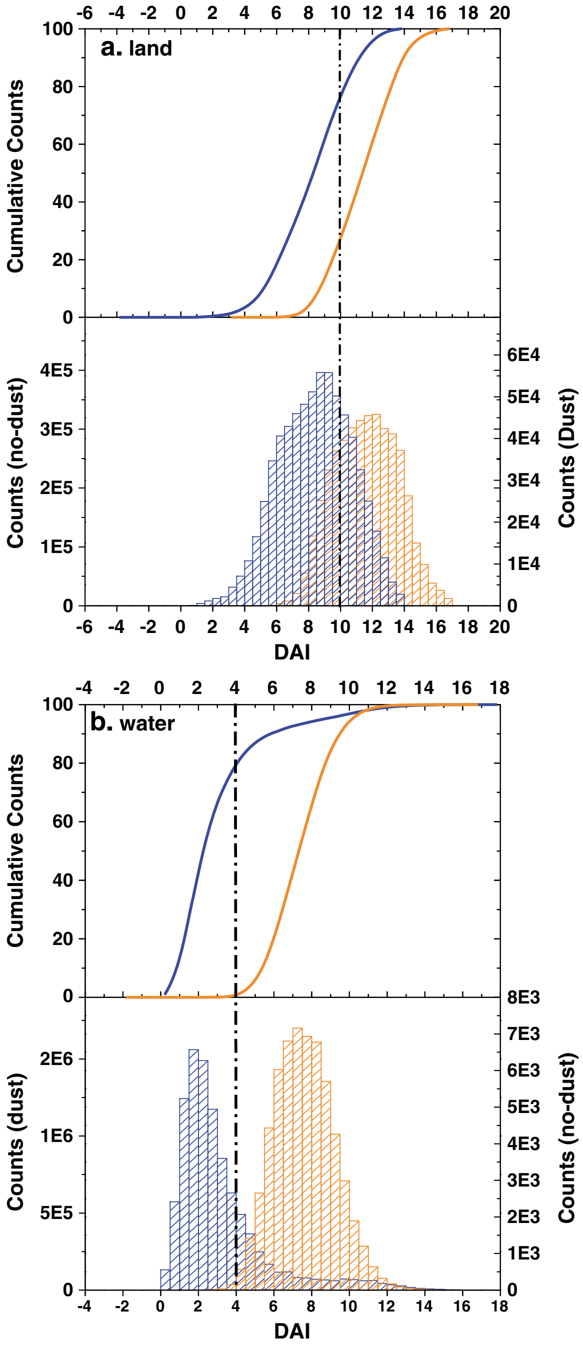

Figure 6. Histograms of DAI for dust-laden pixels (orange) and no-dust pixels (blue). Dash-dotted lines represent the threshold (with a value of 10 for land and 4 for water) of DAI (a) over land and (b) over water.

In equation (2), R is the observed TOA reflectance. The rationale behind this index is that particle size of dust is considerably larger than smoke; therefore, dust extends its scattering signature even to shortwave IR wavelength, whereas smoke is mostly transparent [*Kaufman et al.*, 2000]. Figure 4b shows a scatterplot between TOA reflectance at 412 nm and 2130 nm for pixels identified as smoke, dust, and clear over ocean. One can see that pixels with dust have higher reflectance at 2130 nm and are well separated from clear pixels and pixels with smoke. The NDAI is applied to pixels which pass through the DAI threshold test.

The approach of the DAI-based dust identification algorithm is to determine the optimal thresholds for both DAI and NDAI that will separate dust from other aerosols and surface. As for separating dust from clouds, bright clouds are first removed as a result of the saturation of MODIS deep blue or blue channels over bright target. Thin cirrus detection tests in the MODIS cloud mask is then used to indentify cirrus clouds and a spatial uniformity test is further used to screen out residual cloudy pixels.

To determine thresholds for DAI and NDAI, supervised MODIS granules, from global observations over the time period from 2002 to 2012, containing solely either smoke or dust are used. Figure 5 shows the locations of those granules, indicating a good coverage of regions where smoke/dust events are frequently observed. Note that only observations from Aqua were selected due to the calibration errors in deep blue bands on Terra [*Kwiatkowska et al.*, 2008]. Secondly, both aerosol optical depth (AOD) and Ångström exponent (AE) from retrievals with MODIS deep blue algorithm and AOD, AE, and fine mode weight (FMW) from MODIS C5 products were used, respectively for over land (bright surface) and over water, to identify pixels with dust or smoke. AE is calculated from the spectral dependence of AOD, which is in turn influenced by aerosol size. As dust-dominated aerosol mixtures are dominated by coarse-mode particles, unlike most other common aerosol types, they have characteristic values of AE which allows for some differentiation between dust and nondust aerosols [*Eck et al.*, 1999], As an example of this application, *Hsu et al.* [2006] used AE to identify Asian dust plumes. Details on the criterion used to separate dust (or smoke) from no dust (or no smoke) are given in Table 1. For dust over land, pixels with

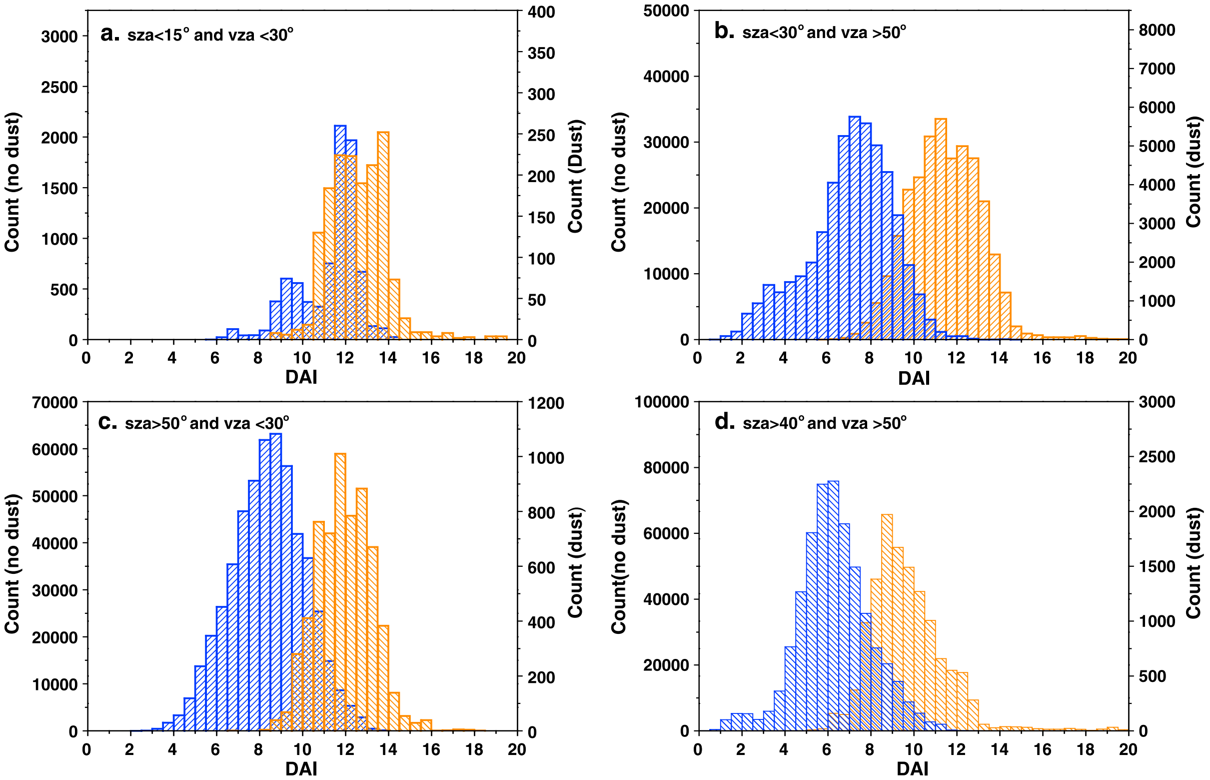

Figure 7. Histograms of DAI for dust-laden pixels (orange) and no-dust pixels (blue) over land in different combinations of SZA and VZA values: (a) SZA <15° and VZA <30°, (b) SZA <30° and VZA >50°, (c) SZA >50° and VZA <30°, and (d) SZA >40° and VZA >50°.

dust are defined as AOD greater than 0.5 (i.e., encompassing from medium to thick dust loading) and AE less than 0.5, as indicated by the aerosol climatology using AERONET Sun photometer data [*Holben et al.*, 2001], clear (no dust) pixels are defined as AOD <0.2 and AE >1.0. For dust over water, pixels with dust are defined as pixels with AOD >0.5, AE <0.5, and FMW <0.3 and clear (no dust) pixels are for pixels with AOD <0.2 and FMW >0.7. Analysis of 10 years of Aqua granules with dust events using these criteria resulted in 12,648 dusty pixels and 9,278 no-dust pixels. Histograms, most importantly, cumulative histograms of DAI were generated from these pixels and are shown in Figure 6. Over land, it is seen that the distribution of dusty pixels is generally well separated from that of clear/no dust pixels. However, an overlap region exists between values at the high end of no-dust pixels and low end of dust pixels. There are in general three factors likely causing this overlap. First one is the uncertainty in the MODIS deep blue AOD and AE, which leads to incorrect classification of dust and no-dust pixels by applying above mentioned criteria. Second one is the changing surface type, which may cause either a larger DAI for clear pixels due to the spectral dependence of surface reflectance or smaller DAI as a result of different dust optical properties. However, the geographical distribution of the granules containing the pixels in the overlap region does not show any specific location or surface type, indicating the effect of this factor is minimal. The third one is the solar and viewing geometry dependence of DAI as shown in Figure 3. By splitting the data used in Figure 6a according to different range of solar and viewing zenith angle into four categories, i.e., (a) SZA <15° and VZA <30°; (b) SZA <30° and VZA >50°; (c) SZA >50° and VZA <30°; and (d) SZA >40° and VZA >50°, histograms of DAI were analyzed and are shown in Figure 7. It is seen that DAI for dusty and no-dust pixels are largely overlapped for category (a) as a result of shifting of no-dust distribution to the higher DAI, implying the difficulty to separate dust from no dust at a lower SZA with a lower VZA, which is consistent with the simulations for over land as shown in Figure 3. The overlap region becomes considerably smaller and clear separation between dust and no dust become evident for other three categories. It is also noted that for category (d), i.e., higher SZA with a higher VZA, the peak of dusty pixels shifts to the lower DAI. The angular sampling of the data shows that ~25% (or ~13%) of dusty (or no-dust) pixels are falling into category (a), while only 1% (or 5%) of dusty (or clear) pixels are within category (d),

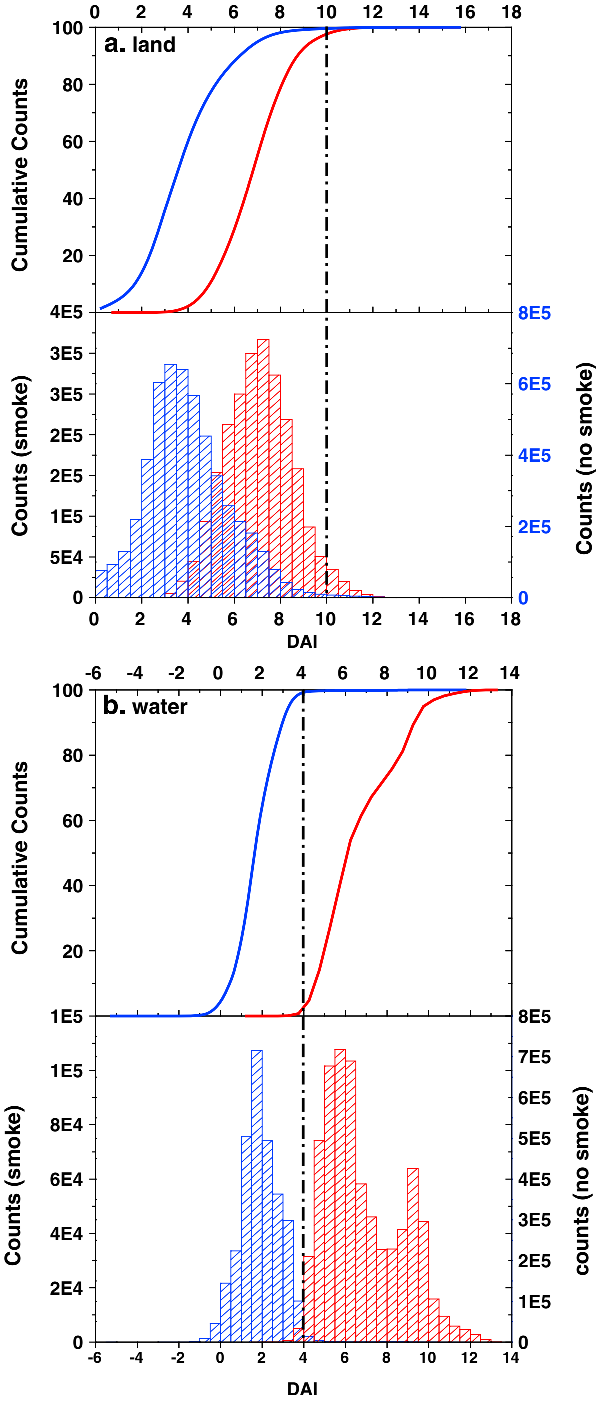

Figure 8. Histograms of DAI for smoke-laden pixels (red) and no-smoke pixels (blue). Dash-dotted lines represent the threshold (with a value of 10 for land and 4 for water) of DAI (a) over land and (b) over water.

i.e., most data are falling into other angular ranges. However, as the cumulative histogram in Figure 6a shows, selecting a DAI threshold of 10, the correct dust detection ratio is at ~70%, and the probability of false detection is ~30%. In addition, the 30% missed detection spread to nearly all granules used to determine the DAI threshold, indicating the threshold used is not affected by specific dust events. However, there is a tendency that large portion of the 30% missed dust is associated with an extreme viewing geometry (higher SZAs and VZAs), as shown in Figure 7d. Compared to over land, the dust and no-dust pixels over water are well separated from each other (shown in Figure 6b), which is in accordance with the simulations shown in Figure 3b. Note that sunglint regions are excluded. There are a very small amount of no-dust pixels with a higher DAI that overlapped with dusty pixels. The lower uncertainty in the MODIS AOD retrievals over ocean and the retrieved FMW for AOD >0.5 give our confidence in selecting a DAI threshold of 4, which leads to ~100% correct detection with a false alarm rate of ~20%.

To determine thresholds for NDAI, 10 MODIS granules with smoke pixels and no-smoke pixels were analyzed. For smoke over land, pixels with smoke were defined as AOD greater than 0.5 (i.e., encompassing from medium to thick smoke aerosol loading) and AE larger than 1.0; clear/no-smoke pixels were defined as AOD <0.2. For smoke over water, pixels with smoke were defined as pixels with AOD >0.5, AE >1.0, and FMW >0.7, and clear/no-smoke pixels were for pixels with AOD <0.2 and FMW<0.3. Histograms of DAI for smoke and no-smoke pixels shown in Figure 8a indicate that DAI for all no-smoke pixels and nearly 95% of smoke pixels are well below the threshold value of 10 over land suggesting that DAI threshold of 10 is able to classify successfully smoke pixels as nondust pixels over land Over water, as shown in Figure 8b about 98% of smoke pixels have DAI values larger than 4, which is the threshold of DAI, i.e., by using DAI alone, nearly all smoke pixels will be classified as pixels with dust.

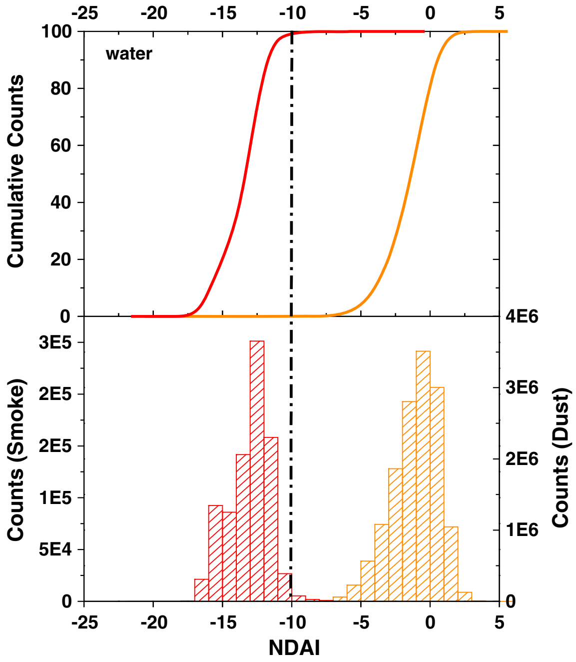

Figure 9. Histogram of NDAI for dust-laden pixels (orange) and smoke-laden pixels (red) over water. Dash-dotted line represents the threshold (with a value of −10) of NDAI.

However, distribution of NDAI (shown in Figure 9) indicates a separation between smoke and dust pixels. By using −10 as NDAI threshold after applying DAI threshold, smoke pixels can be well distinguished from dust pixels over water. The larger difference in DAI between smoke and dust over land are the combined results of the difference in spectral dependence of absorption in deep blue to blue wavelength region between smoke and dust [*Hsu et al*., 2004], and a stronger multiple scattering between surface and atmosphere over land, owing to higher and spectrally increasing surface reflectance. The more absorption by smoke in longer wavelength than that by dust leads to a higher spectral ratio between TOA reflectance at 412 nm and that at 440 nm, consequently a lower DAI. Simulations from *Hsu et al*. [2004] showed that TOA reflectance at 412 nm increases, whereas that at 490 nm decreases when aerosol type changes from pure dust to pure smoke.

Before proceeding to perform dust detection, the algorithm has to identify clouds so those pixels are not processed for detecting dust. The DAI-based dust identification algorithm has three steps to screen for clouds. First, using the saturation in deep blue (410 nm) or blue (420 nm) channels to mask out bright pixels which is usually associated with thick bright clouds. Thick dust is not as bright as a cloud, and the blue channels do not saturate. Second, cirrus cloud tests in MODIS cloud mask are used to mask out the pixels contaminated by cirrus clouds. Third, spatial variability test using 0.86 μm, developed by *Martins et al*. [2002], for over water and 0.41 μm for over land are used to screen out residual clouds.

3. Results

The algorithm was run on multiple MODIS Aqua granules covering different regions and over time periods from 2002 to 2012 to test its performance. A couple of examples involving Asian dust storm and transatlantic dust transport are described in detail below.

3.1. Asian Dust Storm

Dust storms appear frequently over China during spring time and detecting dust from space-borne measurements is useful to track the onset and transport of the dust. The red, green, and blue (RGB) composite and DAI images shown in Figure 10 captured the 3 day dust storm event over China from 11 to 13 May 2011. By comparing the DAI with the corresponding RGB composite images where dust is visibly brown in color, one can see clearly that the DAI captures the evolution of this dust storm event very well. Note that dust mask shown in Figure 10 is given as DAI after subtracting the detection threshold in order to show uniform dust intensity between land and water. On 11 May 2011, large plumes of sand and dust blew out of the Gobi desert and spread across the Mongolia-China border; on 12 May, the plume moved toward northeastern China and covered the provinces of Heilongjiang, Jilin, and Liaoning; and on 13 May, the same plume moved out of China and over to Korean and Japanese sea. Note though that a small part of dust plume over land, such as the left part of dust plume in Figure 10 (left) and the tail of the plume in Figure 10 (middle), are missed by DAI, most probably due to relatively low dust loading. The current version of dust identification

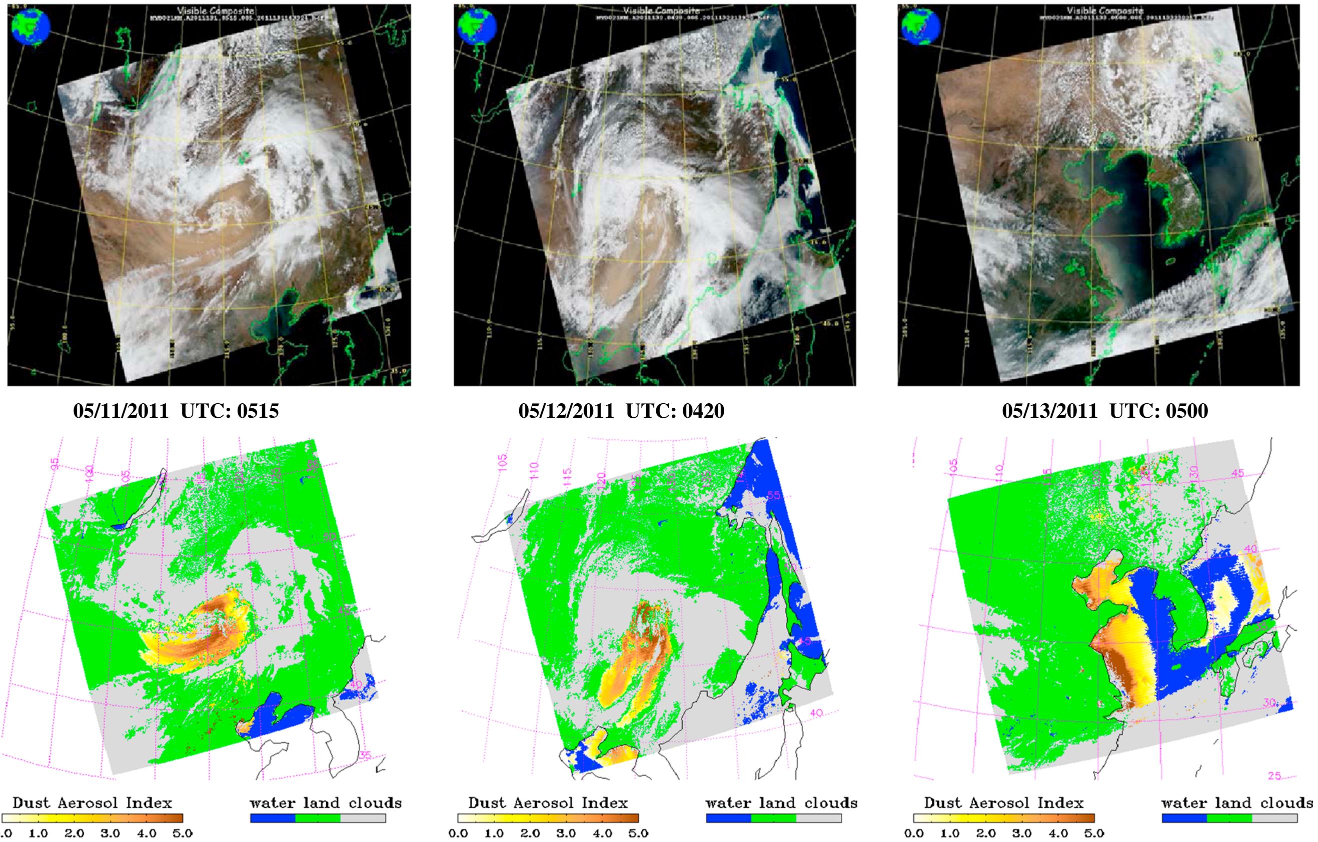

Figure 10. Dust storm over China detected with DAI-based dust identification algorithm. (top) RGB composite image for MODIS Aqua granule on (top) 11 May 2011 (UTC: 0515), (middle) 12 May 2011 (UTC: 0420), and (right) 13 May 2011 (UTC: 0500 UTC), respectively. (bottom) DAI for each corresponding granule.

algorithm is only designed for cloud-free condition, due to which the detection of dust mixed in with clouds is not possible (e.g., plume on the top right corner on 13 May). In addition, it should also be noted that coastal turbid or shallow water shown on Figure 10 (right) is likely falsely indentified as dust by DAI dust identification algorithm, since the threshold of DAI over water was defined according to a dark ocean surface. This problem

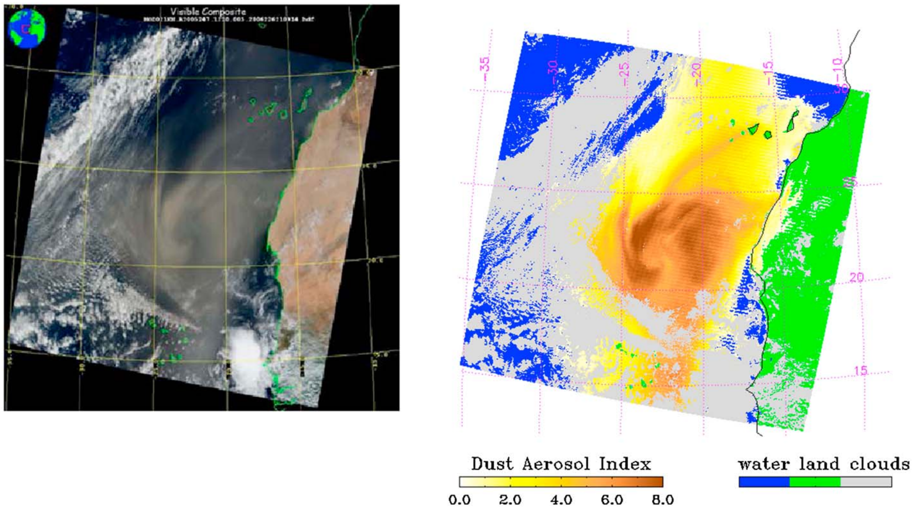

Figure 11. Dust outbreak over coastal West Africa on 4 September 2004 at 1210 UTC. (left) MODIS RGB composite image and (right) DAI image.

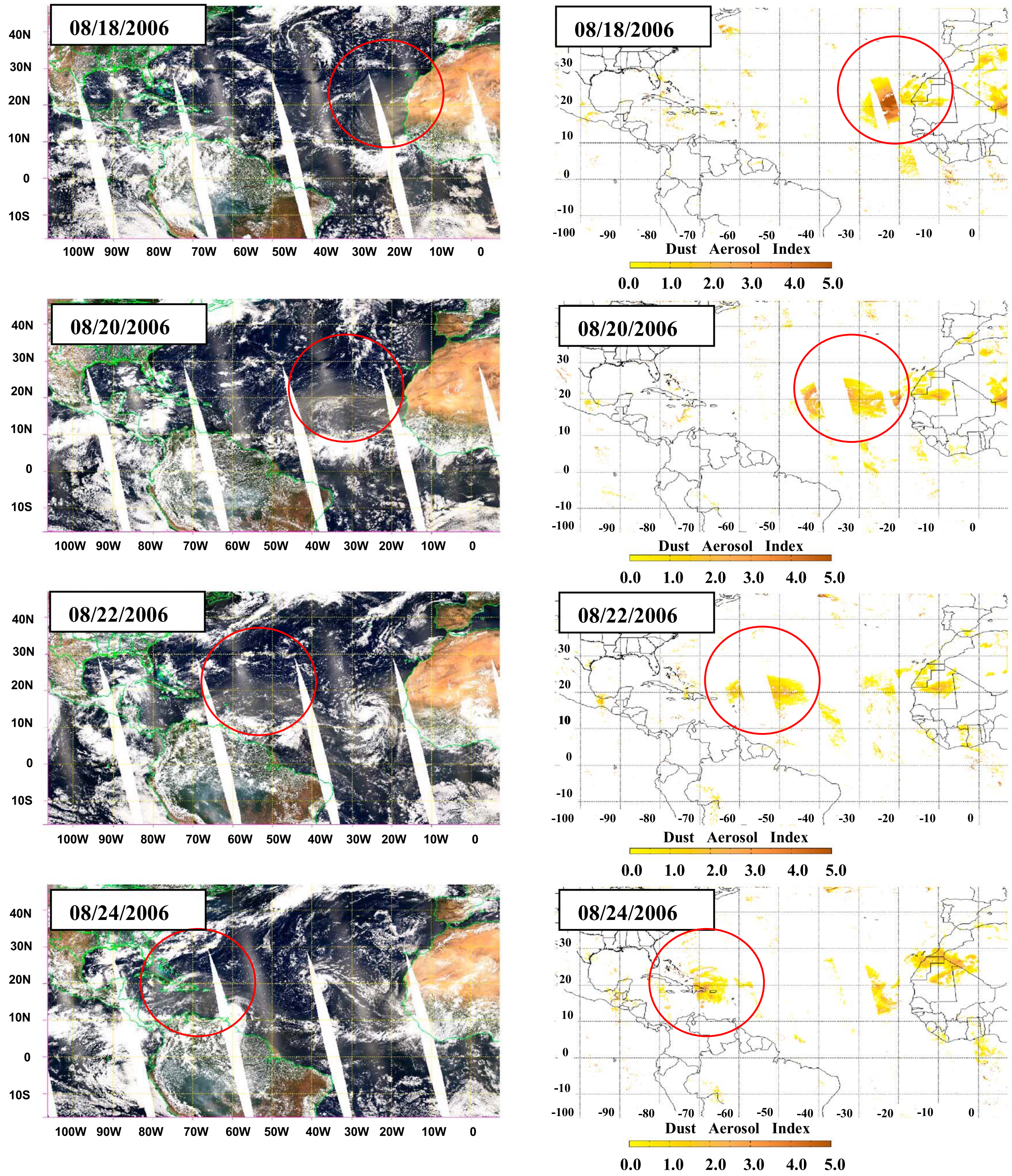

Figure 12. (left) RGB composite images and (right) DAI images over the Atlantic Ocean for 18, 20, 22, and 24 August during a transatlantic dust event for eight consecutive days from 17 to 24 August 2006.

can be handled by using turbid water test, such as those used frequently in ocean color products [*Shi and Wang*, 2007] or sediment mask, such as the one proposed by *Li et al.* [2005].

3.2. Transatlantic Dust Transport

Compared to dust over land, dust over water is relatively easy to detect with the DAI-based dust identification algorithm due to the low and spectrally flat surface reflectance. The RGB composite image in Figure 11 (left) shows dust outbreak from West Africa that spreads over the ocean on 4 September 2005. This outbreak is clearly captured in DAI shown in Figure 11 (right). Besides the extent of the dust plume, DAI can also perfectly illustrate the distribution of the intensity or thickness of the plume. Additionally, not only the outbreak but also the transport of dust can be monitored. As an example, DAI-based dust identification algorithm was applied to the MODIS Aqua observations over the same time period and area for an event reported by *Liu et al*. [2008]. In their study, this transatlantic dust transport event was clearly identified by using a series of CALIOP observations for the time period from 17 to 24 August 2006. Both RGB composite images and DAI for four selected days, i.e., on 18, 20, 22, and 24 August, during the same time period are shown in Figure 12. Note that as we discussed in section 2, sunglint will also cause high DAI values, and the glint location varies with viewing and illumining geometry. Due to gaps associated with sunglint, the coverage of dust plume is sometimes irregular. One can clearly see from Figure 12 that dust plume, as highlighted by high DAI values in the circle and the corresponding circle in RGB composite images, moved from West Africa to America during these 8 days. And, the location and time of this dust plume movement shown in Figure 12 is in accordance with the results from CALIOP observations shown by *Liu et al*. [2008].

4. Evaluation of DAI-Based Dust Identification Algorithm

4.1. Validation With CALIOP Vertical Feature Mask Product

The Cloud-Aerosol Lidar and Infrared Pathfinder Satellite Observation (CALIPSO) is one of the constellation satellites in the EOS A-Train formation that was launched in April 2006 [*Winker et al*., 2009, 2010]. CALIPSO combines an active Cloud-Aerosol Lidar with Orthogonal Polarization (CALIOP) with passive infrared and visible imagers to probe the vertical structure and properties of thin clouds and aerosols over the globe. Besides cloud type, CALIOP onboard the CALIPSO satellite also identifies aerosol types including smoke and dust. Vertical Feature Mask (VFM) is one of the CALIOP products which give aerosol types and their vertical locations with a resolution of 330 m spatially and about 16 tracks globally once during the day and once during the night. Aerosol typing in CALIOP VFM product has been compared with both ground-based AERONET observations [*Mielonen et al*., 2009] and airborne High Spectral Resolution Lidar (HRSL) [*Burton et al*., 2013]. It was indicated that the agreement with HSRL and AERONET was at 80% and 91%, respectively. This gives us confidence to use VFM as one of the “truth” data for quantitative evaluation of the performance of the DAI-based dust identification algorithm. However, it also should be noted that CALIOP data have a lower signal-to-noise ratio during daytime [*Vaughan et al*., 2009], and there is a larger possibility of misclassification of aerosols as clouds since VFM is generated at the downstream of the cloud-aerosol discrimination scheme [*Liu et al*., 2009].

The DAI-based dust identification algorithm applied to MODIS observations has 1 km resolution. VFM data are divided into 5 km chunks along CALIOP track with 15 profiles in each chunk. To generate the matchup data set, only the three middle profiles in each CALIOP VFM 5 km chunk are used with a restriction on the time difference between the center of the selected VFM profiles and MODIS granule UTC time to within ±5 min; MODIS pixels within ± 500 m of the center of the three selected CALIOP profiles are used. To determine the dominant aerosol type in VFM, all three VFM profiles are first required to be cloud free in any vertical layer between 0 and 12 km. Second, dust, smoke, and other aerosol fraction, i.e., number of dust (or smoke, or other aerosol) layer divided by the total number of aerosol layers from surface to 12 km for each profiles are calculated, and dominant aerosol type for each profile is defined as the type with the largest fraction. Finally, the feature is chosen as dominant feature if this feature is dominant in two out of the selected three VFM profiles.

Similar to validation of many other discrete (binary yes/no) retrievals [*Ramirez-Beltran et al*., 2008; *Wilks*, 1995], the performance of the MODIS DAI algorithm is also evaluated using a contingency table. The variable a represents true positives, the number of matchups where both VFM and DAI algorithms indicate the presence of “dust”; the variable b represents false positives, the number of times where VFM indicates “no dust,” but DAI algorithm indicates “dust”; the variable c represents false negatives, the number of times where VFM indicates “dust,” but DAI algorithm indicates “no dust”; the variable d represents true negatives, the number of times where both VFM and DAI algorithms indicate “no dust.” The conventional statistical matrix to measure the retrieval performance consists of three metrics, i.e., accuracy, Probability Of Correct positive Detection (POCD), and Probability Of False positive Detection (POFD). They are defined as follows:

$$\text{Accuracy}(\%) = \frac{a+d}{a+b+c+d} \times 100 \tag{3}$$

$$\text{POCD}(\%) = \frac{a}{a+c} \times 100 \tag{4}$$

$$\text{POFD}(\%) = \frac{b}{a+b} \times 100 \tag{5}$$

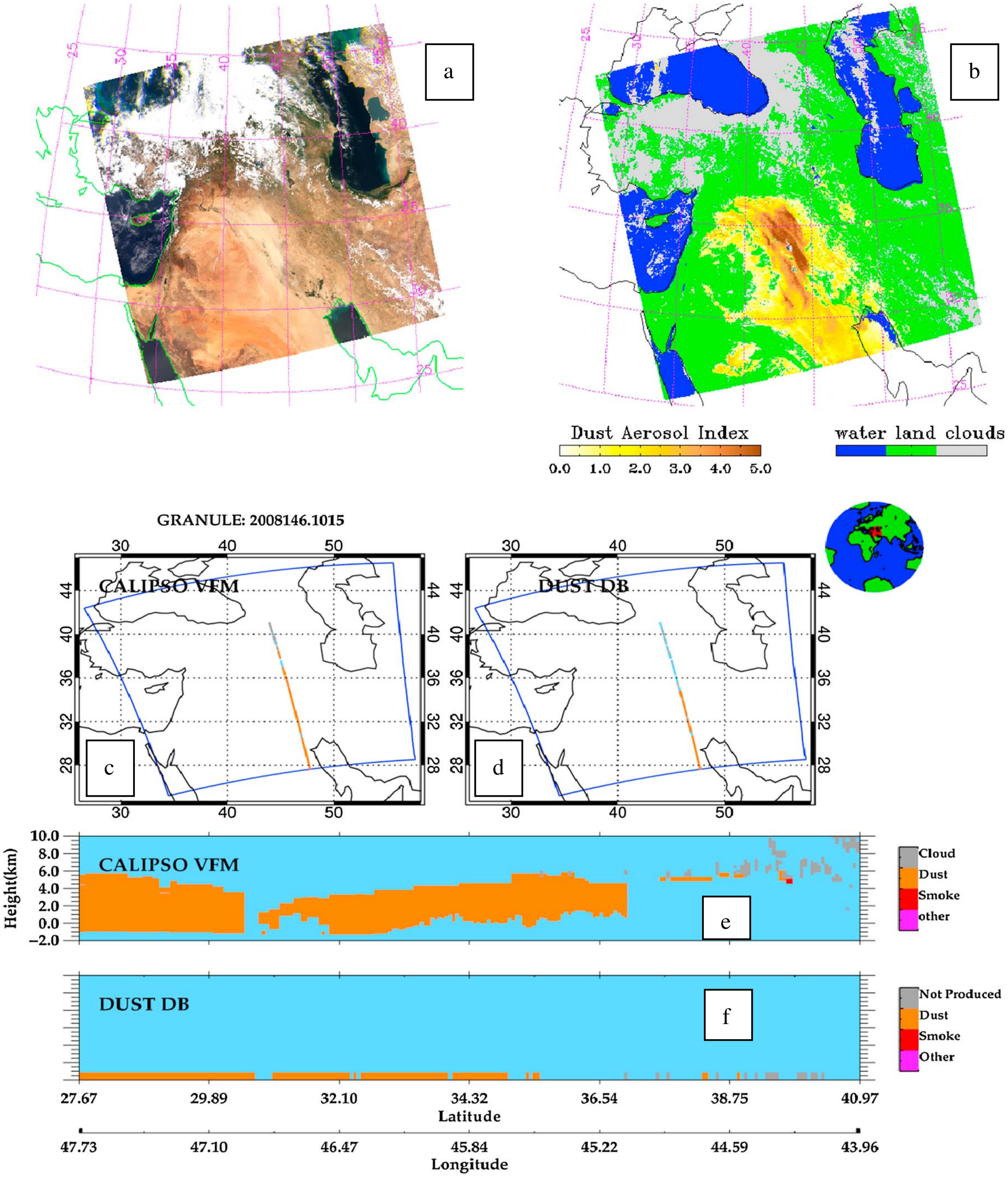

Figure 13. Comparison of dust detected with DAI-based algorithm with aerosol types in CALIOP Vertical Feature Mask (VFM) on 25 May 2008 at 10:15 UTC. (a) RGB composite image, (b) DAI, (c) aerosol types on CALIPSO track with dust (orange), clouds (gray), smoke (red), clear (light blue), and other type of aerosol (pink), (d) DAI on CALIPSO track, (e) vertical distribution of aerosol types on the part of CALIPSO track collocated with MODIS DAI, and (f) DAI between 0 and 2 km for illustration purpose on the same part of track as in Figure 13e.

Figure 13 shows one example of a matchup between detection from MODIS DAI-based dust identification algorithm and CALIOP VFM product in one MODIS granule. From RGB composite image (Figure 13a), it is seen that there is a dust storm outbreak in Saudi Arabia and Iraq desert. And DAI algorithm successfully captured this event (Figure 13b). Fortunately, one CALIOP track passed through this granule with a time difference less than 5 min, which enabled us to calculate the metrics to evaluate the DAI-based dust identification algorithm. The collocated path and the dominant features on each collocated location from both VFM and detection from MODIS DAI-based algorithm are given respectively in Figures 13c and 13d. The vertical distribution of dust, cloud, and other features from VFM are shown in Figure 13e. Such information can be used to verify the sensitivity of DAI-based dust identification algorithm to the height of the dust layer. For the purpose of comparison, the detected dust, cloud, and clear condition from DAI-based algorithm is also shown in Figure 13f, which is a similar plot as Figure 13e, but with features artificially laid from 0 to 2 km for the sake of illustration. A total of 222 matchups were obtained for this case shown in Figure 13. The accuracy, POCD, and POFD are 86.6%, 84.1%, and 6.9%, respectively, indicating a very good agreement between DAI and CALIOP VFM product for this matchup.

By applying DAI-based dust identification algorithm over global MODIS Aqua granules for all the dust events observed between 2006 and 2012 and collocating with available CALIOP VFM products, a total of 18,358 matchups (15,477 and 2,881, respectively for over land and water) in 112 granules were obtained. Dust events were identified from NASA MODIS Land and Atmosphere Near Real-Time Capability for EOS (LANCE) website located at http://rapidfire.sci.gsfc.nasa.gov/gallery/. Note that this analysis does not include the data used to determine DAI and NDAI thresholds. The ensemble of accuracy, POCD, and POFD were assessed according to surface type, and they are 70%, 80%, and 49% for over land, and 82%, 76%, and 18% for over water (Table 2). The POCD and POFD are very close to theoretical values that were derived for the selected thresholds (see Figure 6) for both over land and water. In general, dust detection with DAI-based algorithm has a good performance for both over land and water, or even better when taking into account of the accuracy of CALIOP VFM product itself, as we discussed above. And, higher accuracy and lower false alarm over water than those over land were clearly seen, owing to the relative lower, spectrally flat and more homogeneous surface reflectance over water in the deep blue and blue wavelength region. Over land, some surface types, such as bright desert, pose sharp increase of surface reflectance with increasing wavelength in the deep blue to blue region, as shown by *Hsu et al.* [2004], which tends to falsely classify some bright

Table 2. Statistics Metrics for Comparisons of DAI-Based Dust Identification Algorithm Against CALIOP VFM Product[a]

Surface Type		Number of Matchups				Accuracy	POCD	POFD
		True Positive *a*	False Negative *c*	True Negative *d*	False Positive *b*	$(a+d)/(a+b+c+d)$ (%)	$a/(a+c)$ (%)	$b/(a+b)$ (%)
Land	all	3759	901	6790	3716	70.0	80.6	49.7
	B_height >0.5 km	1014	298	1706	1464	67.6	77.3	-
	B_height >1.5 km	397	106	1706	1464	66.9	78.9	-
	B_height >3.0 km	146	13	1706	1464	66.7	91.8	-
	D_thick >0.5 km	786	250	1706	1464	59.2	75.8	-
	D_thick >2.0 km	535	125	1706	1464	58.5	81.0	-
	D_thick >3.0 km	282	54	1706	1464	54.7	83.9	-
Water	all	871	274	1356	204	82.3	76.1	18.9
	B_height >0.5 km	91	53	1269	128	88.3	63.2	-
	B_height >1.5 km	45	45	1269	128	88.3	50.0	-
	B_height >3.0 km	25	37	1269	128	88.7	40.3	-
	D_thick >0.5 km	85	30	1269	128	69.7	73.9	-
	D_thick >2.0 km	64	28	1269	128	68.9	69.5	-
	D_thick >3.0 km	40	10	1269	128	69.8	80.0	-

[a] B_height: the height of lowest dust layer identified in CALIOP VFM product. D_thick: the thickness of total dust layer in VFM product, i.e., height of the top dust layer − height of the bottom dust layer in the profile.

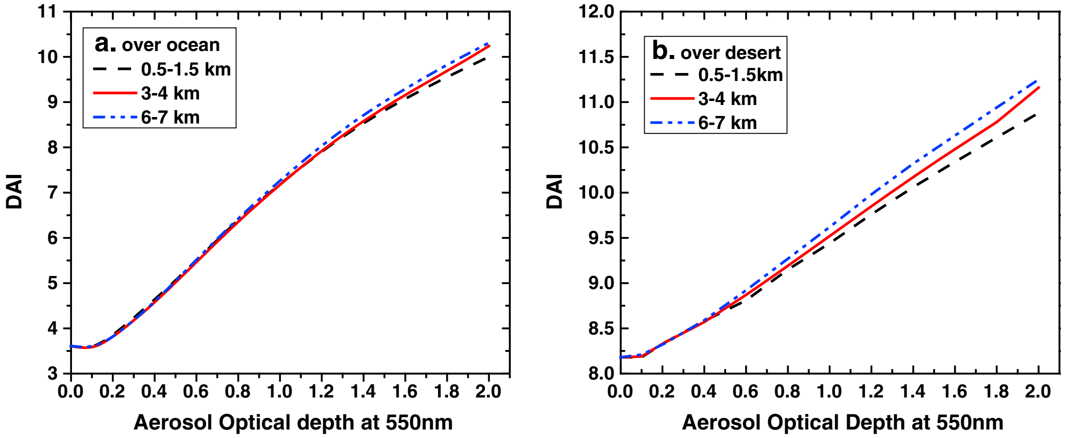

Figure 14. DAI for dust layer spreading between 0.5 km and 1.5 km (black dashed line), between 3 km and 4 km (red solid line), and between 6 km and 7 km (blue dash-dotted line) as a function of aerosol optical depth at 550 nm. (a) Over ocean and (b) over desert. Both solar zenith angle and viewing zenith angle are set at 30°. Relative azimuth angle is set at 120°. Total column of ozone amount is set at 350 DU.

surfaces as dust, leading to a larger POFD. This might be mitigated in the future by computing a bright pixel index using normalized index of reflectances at 1.24 μm and 2.15 μm which will flag bright surfaces when there is no dust in the atmosphere and downgrading the confidence in the dust detected over those bright pixels. Preliminary testing shows that the normalized difference vegetation index (NDVI)-based bright pixel index is expected to reduce the false alarms substantially.

CALIOP VFM product provides the vertical profile of the identified aerosol types, which can be used to investigate the sensitivity of DAI-based algorithm to both the height and thickness of the dust layer. To this end, we stratified the performance metrics according to the height of the lowest dust layer identified by CALIOP VFM product for three scenarios, i.e., including only dust cases with layers higher than 0.5 km, 1.5 km, and 3 km, but with a thickness between 1.0 and 2.0 km, to isolate the effect from changing thickness of dust layers. Similarly, we separated the matchups between detections from DAI-based algorithm and CALIOP VFM into three groups according to the total thickness of dust layers, i.e., including only dust cases with a thickness larger than 0.5 km, 2 km, and 3 km, but only with the bottom layer height between 1.0 and 2.0 km for the same reason as to isolate the effect from the changing elevation of dust layer. Number of incidences for each category in contingency table, and corresponding accuracy, and POCD are given in Table 2 for over land and ocean. The reason that we did not include POFD is that the change of POFD has no physical meaning according to the definition of POFD. Over land, it is shown that, compared to a scenario that includes both near-surface and high-altitude dust layers, including only the elevated dust layers has negligible effect on accuracy but increases POCD by ~18% . Similarly, including only thick dust layers (with a thickness larger than 3 km) increases POCD (~10%). Over water, it is shown that there is a tendency that an increased dust layer thickness increases POCD, while elevating dust layer height indicates a slight reduction of POCD; however, the number of samples are also significantly reduced (less than 60).

To understand the sensitivity of the dust detection with DAI-based algorithm to the height of dust layer, we simulated the effect of changing dust layer height on DAI with 6S, respectively for over an ocean surface and desert surface. In the simulations, dust layer was spread exponentially between 0.1 and 1.5 km, 3 and 4 km, and 6 and 7 km, respectively, for different AOD values between 0 and 2.0. Figure 14a shows DAI as a function of AOT for dust layer spreading between 0.5 km and 1.5 km (black dashed line), between 3 km and 4 km (red solid line), and between 6 km and 7 km (blue dash-dotted line) over ocean. Although DAI increases with AOD as expected, the height of the dust layer has no bearing on DAI; the increase in DAI with dust aerosol height for the same AOD is marginal. This implies that the ability to detect dust is the same irrespective of the aerosol height and in agreement with analysis reported in Table 2. As shown in Figure 14b, over land, however, the height of dust layer has a small effect on DAI. DAI is higher when dust aerosol layer is higher implying dust detection is enhanced when aerosol layer

Table 3. Statistical Metrics for DAI, LDA, QDA, and MCI Algorithm Against CALIOP VFM Products[a]

Surface Type	Algorithms		Accuracy (%)	POCD (%)	POFD (%)
Land	DAI		70.0	80.6	49.7
	DA	QDA	-	-	-
		LDA	-	-	-
	MCI		63.6	44.1	74.2
Water	DAI		82.3	76.1	18.9
	DA	QDA	85.6	83.8	22.9
		LDA	80.8	63.6	18.9
	MCI		66.1	59.5	25.4

[a] DA: discriminant analysis method; LDA: linear discriminant analysis method; QDA: quadratic discriminant analysis method; MCI: multichannel imager method; DAI: DAI-based dust identification algorithm.

is high compared to near the surface. This is also consistent with analysis presented in Table 2. *Hsu et al.* [2004] have also shown that deep blue wavelength is less sensitive to variations in aerosol height than UV wavelength, as a result of a smaller Rayleigh scattering effects.

To show the advantages and disadvantages of the DAI-based dust identification algorithm, two other existing algorithms were selected and applied for the same MODIS granules used in above validation, and the corresponding statistical metrics were derived against the exact same matchups with CALIOP VFM as shown in Table 2. The two algorithms are linear (or quadratic) discriminant analysis (LDA or QDA) method [*Cho et al.*, 2013] and multichannel imager (MCI) algorithm [*Zhao et al.*, 2010]. The former one is based on complex statistics and pattern recognition method by using the combined visible and infrared MODIS radiative parameters from six latitude bands and four seasons. Note that it is for detecting optically thin dust over ocean only and trained with a collocated one year MODIS and CALIPSO data sets. Same as DAI-based dust identification algorithm, the latter one is for both land and water and based on universal thresholds, but by relying on a combination of various visible spectral contrast and spatial variability tests with IR brightness temperature difference test. Table 3 gives statistical metrics of these two algorithms together with the DAI-based dust identification algorithm. Over ocean, it is clearly seen that both LDA (or QDA) method and DAI-based dust identification algorithm have comparable accuracy, POCD, and POFD but perform much better than MCI algorithm since MCI is optimized for thick dust plumes and the CALIOP VFM matchups used here are dominated by thinner and intermediate dust layers or plumes. The accuracy, POCD, and POFD are 85(or 80)%, 84(or 60)%, and 22(or 18)% for LDA(or QDA) method and 82%, 76%, and 18% for DAI-based dust identification algorithm, while MCI algorithm has 66%, 59%, and 25%, respectively. Over land, DAI-based dust identification algorithm performs much better than MCI algorithm, with accuracy, POCD, and POFD of 70%, 80%, and 48%, respectively. The corresponding values for MCI are 64%, 44%, and 74%. The difference between DA methods and MCI has been discussed by *Cho et al.* [2013]. If MCI algorithm developers relax thresholds for their algorithm to include intermediate dust scenarios, the results of MCI could be different. In the next section, we focus only on comparisons against DA methods.

Although comparisons against CALIOP VFM matchup indicated that DAI-based dust identification algorithm has a comparable performance with LDA (or QDA) method, both algorithms have their own strengths and weaknesses. Some of the advantages and disadvantages cannot be shown in the comparisons against CALIOP VFM matchups, since a very few matchups crossed over thick dust plumes, and a possibility exists for thick dust plumes to be classified as clouds in CALIOP VFM [*Liu et al.*, 2009]. Besides working both over land and water, DAI-based dust identification algorithm has the strength to detect thicker dust, since DAI becomes larger for thicker dust as shown both in observations (see Figures 10 and 11) and simulations (see Figure 3), while LDA (or QDA) has the tendency to miss optically thick dust layers [*Cho et al.*, 2013]. As one example, Figure 15 shows one thick dust plume over Mediterranean Sea originated from Africa on 23 February 2007. It is clearly seen that LDA (Figure 15c) completely misclassified the thick dust plume as cloud. QDA (Figure 15d) picked up slightly more dust but not well organized as the dust plume shown in RGB composite image (Figure 15a). In contrast, DAI-based dust identification algorithm is able to capture not only the thick dust plume over ocean but also the origin of this plume over land very well (Figure 15b). It shows the higher DAI values, associated with the thick plume over ocean.

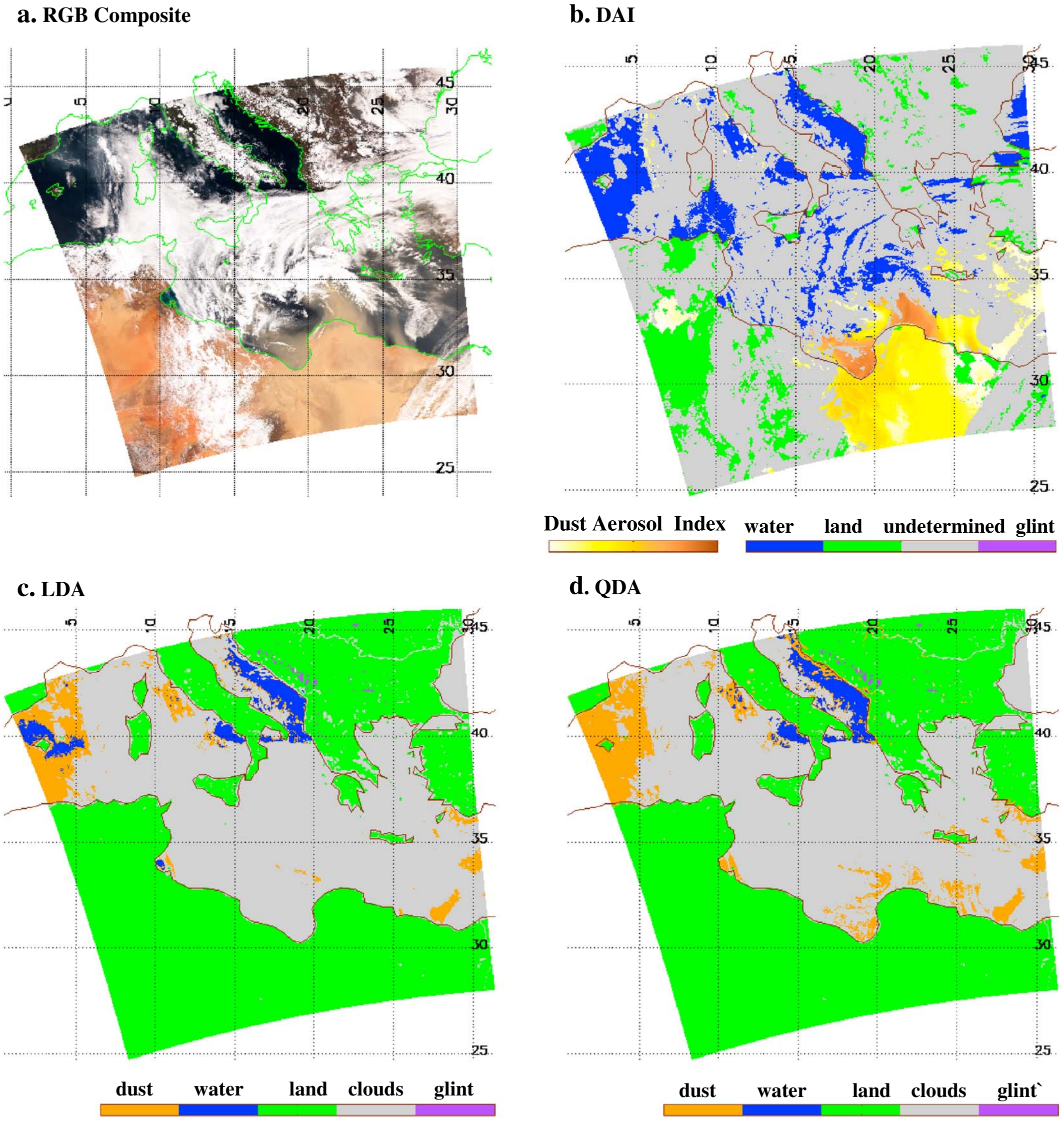

Figure 15. Dust detection results for a thick dust plume over Mediterranean Sea originated from Africa on 23 February 2007. (a) MODIS Aqua RGB composite image at UTC of 12:00, (b) DAI-based dust identification algorithm, (c) LDA method, and (d) QDA method.

However, on the upper left corner of the granule, both LDA and QDA show the presence of dust, while DAI indicates no dust. Significant low concentration of aerosol is indicated over this corner by low aerosol optical depth from MODIS-C5 (less than 0.2), which is the limit of DAI-based dust identification algorithm. Second, as discussed in above sections, DAI-based dust identification algorithm is designed to separate other absorbing aerosols, such as smoke plumes, from dust, while LDA (or QDA) is not optimal for separating smoke plume from dust. One example is given in Figure 16, which shows a large smoke plume over Mediterranean Sea from fires in Greece on 25 August 2007 and is clearly seen in RGB composite image from Aqua MODIS at 12:05 UTC (Figure 16a). Also, as corroborative evidence of smoke, an image with an elevated concentration of total column carbon monoxide from Atmospheric Infrared Sounder (AIRS) which is on the same platform as MODIS Aqua is shown in Figure 16b. Figure 16c shows the results of DAI-based dust identification algorithm applied for this granule. Dust is indicated by light yellow to brownish color (scaled with actual DAI value subtracting the DAI threshold) for any pixel, which passed DAI threshold test but failed NDAI test. However, if any pixel passed DAI threshold and also NDAI threshold test, a nondust absorbing aerosol is indicated and is given in pinkish to red color

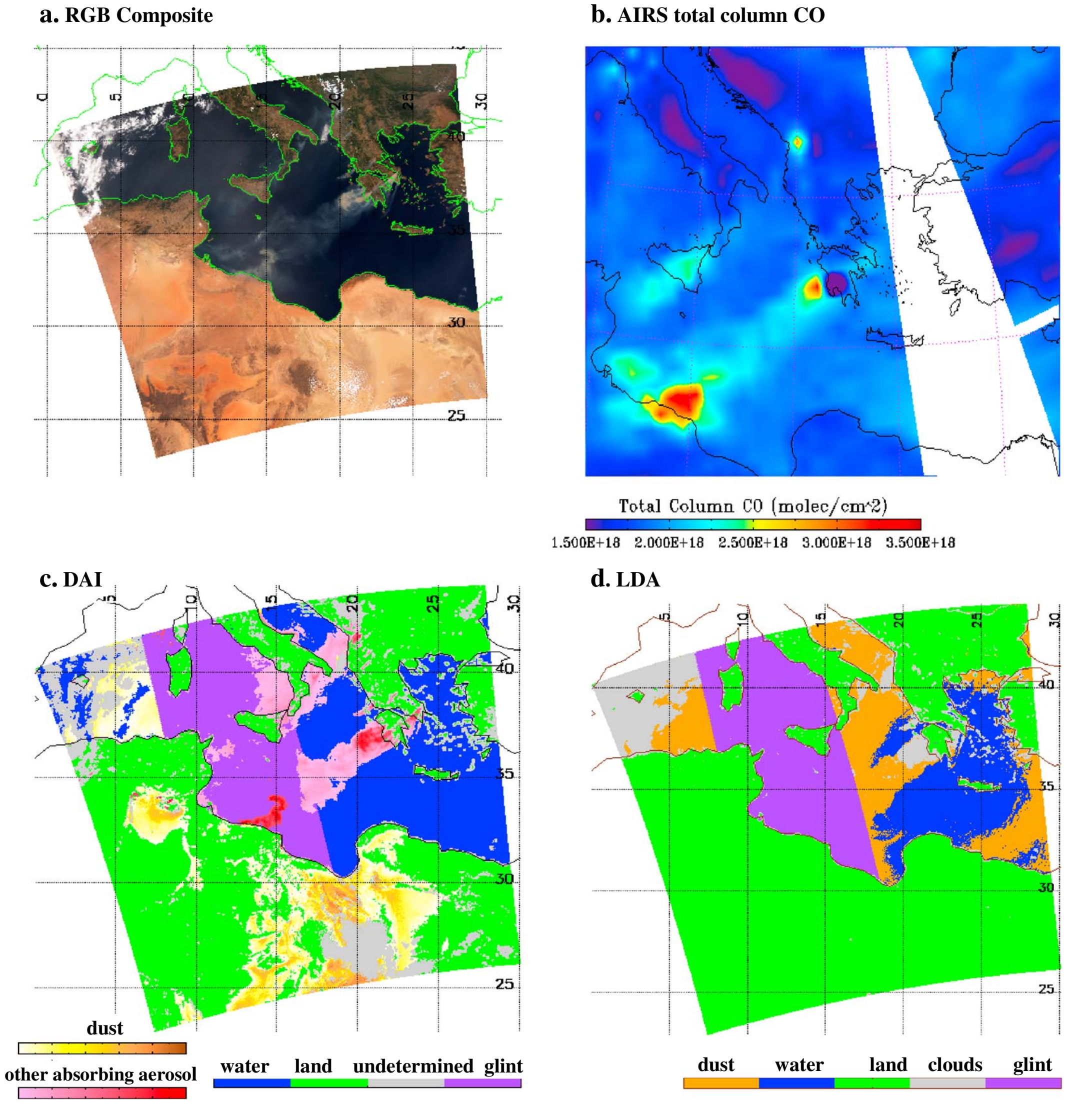
a. RGB Composite

b. AIRS total column CO

c. DAI

d. LDA

Figure 16. Smoke plume over Mediterranean Sea originated from fires in Greece on 25 August 2007. (a) MODIS Aqua RGB composite image at UTC of 12:05, (b) AIRS total column CO, (c) DAI-based dust identification algorithm, and (d) LDA method.

(scaled with actual DAI value subtracting the DAI threshold). It is clearly seen that DAI-based dust identification algorithm correctly classified smoke plume as other absorbing aerosol instead of dust, even inside the sunglint region. Whereas LDA, shown in Figure 16d, misclassified thick smoke plume as cloud and thin smoke plume as dust. QDA shows the same results as LDA. Same as in Figure 15, LDA (or QDA) identified more dust in the region where AOD is very low, as it is claimed that LDA (or QDA) works better for optically thin dust [*Cho et al.*, 2013].

4.2. Comparison With AERONET Observations

The Aerosol Robotic Network (AERONET) [*Holben*, 1998] is composed of automated Sun-sky scanning spectral radiometers that determine AOD by direct Sun measurements. AERONET measurements also provide the Ångström exponent (AE), which is often used to identify if an aerosol type is dominated by small particles, such as smoke, or by larger particles, such as dust [*Dubovik et al.*, 2002, 2006]. In this study, we used level 2.0 AERONET data [*Smirnov et al.*, 2000] from 13 stations (see Table 4), which cover regions not only with frequent dust outbreaks but also regions affected by transported dust, during the time period from the year of 2005 to 2009, to evaluate the accuracy of dust detection with DAI.

Table 4. Statistical Metrics for Comparisons of DAI-Based Dust Identification Algorithm, LDA, and QDA Algorithm Against AERONET Observations[a]

Station	Latitude/Longitude	Height (asl)	True Positive *a*	False Positive *b*	False Negative *c*	True Negaitive *d*	Accuracy (%)	POCD (%)	POFD (%)
Agoufou	15.34°N/1.48°W	305 m	164	22	44	113	80.7.	78.8	11.8
Banizoumbou	13.54°N/2.67°E	250 m	109	5	127	191	69.4.	46.2	4.3
Birdsville	25.90°S/139.3°E	46.5 m	42	24	32	7	46.7	56.7	36.4
Cape San Juan	18.38°N/65.62°W	15 m	9	3	0	8	77.2 72.7[b] 72.7[c]	100.0 77.7[b] 88..9[c]	25.0 12.5[b] 20.0[c]
Capo Verde	16.73°N/22.94°W	60 m	70	12	9	44	84.4 75.6[b] 80.0[c]	88.6 94.4[b] 100.0[c]	14.6 20.9[b] 20.0[c]
Dakar	14.48°N/16.96°W	0 m	189	39	41	93	77.9 65.3[b] 70.8[c]	82.1 85.2[b] 96.5[c]	17.1 27.6[b] 27.2[c]
Dalanzadgad	43.57°N/104.42°E	205 m	42	12	7	25	77.9	85.7	22.2
Djougou	9.76°N/1.59°E	400 m	8	3	17	28	44.6	32.0	27.7
DMN_Maine _Soroa	13.22°N/12.02°E	350 m	61	20	54	88	66.8	53.0	24.6
IER_Cinzana	13.27°N/05.93°E	285 m	62	5	94	141	67.2	39.7	7.4
Saada	31.62°N/08.15°W	420 m	19	30	28	102	67.6	40.4	61.2
Solar Village	24.90°N/46.39°E	764 m	194	117	30	44	61.8	86.6	37.6
Tinga Tingana	28.97°S/139.9°E	38 m	87	45	35	11	55.1	71.3	34.0
Total			1056	324	518	895	69.8	67.1	23.4

[a] asl = above sea level.
[b] LDA method.
[c] QDA method.

As a first step, AERONET measurements are collocated with DAI-based dust identification algorithm applied to MODIS Aqua observations, both temporally and spatially. For AERONET, valid measurements within ±15 min of satellite overpassing time were averaged. For DAI, a circle centered at AERONET station site with a radius of 25 km was selected, and if more than half of the cloud-free pixels within this circle were identified as dusty, then the area within the 25 km radius is considered as dusty. Second, a dust criterion, i.e., AOD at 1020 nm >0.3 and AE between 440 nm and 870 nm <0.6, was used to classify AERONET observations [*Dubovik et al*., 2002]. This criterion is the same as that used by *Schepanski et al*. [2007] but stricter (in terms of AOD) than those used by *Klüser and Schepanski* [2009] and suggested by *Dubovik et al*. [2002] to ensure only dust but not sea salt is included.

As shown in Table 4, a total of 2664 matchups were obtained, and the ensembles of accuracy, POCD, and POFD for the selected 13 stations over 5 year time period are 70%, 67%, and 22%, respectively. Time series analysis of detection with DAI-based algorithm collocated with AERONET AOD as a function of the day of year 2006 for Agoufou site shows that DAI-based algorithm detects dust whenever AODs are high, and the correct detection of the absence of dust by DAI is generally associated with time periods when AOD is low. The performance metrics vary from station to station with accuracy ranging between 47% and 85%. Similarly, POCD values range between 40% and 87%. The lower POCD and accuracy values are generally for stations where number of matchups is not high (Table 3). Three coastal or island stations, i.e., Capo Verde, Dakar, and Cape San Juan, show very high POCD, from 82 to 100%, and lower POFD, from 14 to 25%. Note that Cape San Juan is usually affected by the transatlantic dust. This finding is in accordance with the theoretical analysis of dust detection with DAI, which indicates that DAI usually performs better over water. The two stations over Australia, i.e., Birdsville and Tinga Tingana, however, have generally lower accuracy and higher POFD, indicating DAI thresholds may have regional dependence as a result of different surface type and consequently different optical properties of dust. The one Asian station, Dalanzadgad, does not have great matchups but gives very high accuracy, POCD, and lower POFD. For station located at the center of desert, such as Solar Village, has higher POCD (~86%) but higher POFD (as high as ~37%) as well. In general, the variability of the performance of DAI-based dust detection over the selected stations may suggest future improvement of the algorithm by using geographic and surface-type dependent thresholds.

In addition, matchups between dust detection results with LDA/QDA method and AERONET observations were also obtained for the three coastal or island stations, i.e., Capo Verde, Dakar, and Cape San Juan. The statistical metrics are shown in Table 4 as well. It is seen that both LDA/QDA and DAI-based dust identification algorithm have a higher POCD and relatively lower POFD. The POCD is 77 to 100% for LDA (88 to 97% for QDA), while POFD is around 12 to 27% for both LDA and QDA over these three stations. Compared with results in DAI-based dust identification algorithm, LDA/QDA has a comparable both POCD and POFD.

5. Discussions and Conclusions

In this paper, an algorithm to detect dust using measurements in the deep blue, blue, and shortwave IR spectral region is presented. The decrease in contrast between deep blue (412 nm) and blue (440 nm) relative to a pure Rayleigh atmosphere as a result of dust absorption allows the detection of dust in the atmosphere. Additionally, the large particle size of dust compared to other absorbing aerosols (smoke, etc.) extends its signal from deep blue to near-IR region, which allows the separation of dust from nondust aerosols. The optimal thresholds of DAI for separating dust from no dust and thresholds of NDAI for distinguishing smoke from dust were obtained by analyzing MODIS data for dust and smoke events over a time period of 10 years.

Using several case studies involving formation and transport of dust storms in China and the Atlantic Ocean, it is shown that the algorithm captures the dust events with good performance metrics. Although quantitative evaluation of DAI-based dust identification algorithm is challenging because ground truth is not available, an evaluation approach using CALIOP and AERONET observations is used to demonstrate algorithm performance. It is shown that POCD can reach up to 82% over land and 76% over ocean. The high accuracy and POCD gives confidence in the robustness of the DAI-based dust identification algorithm. However, in the CALIOP comparisons, POFD is higher over land (~50%) than over water (~18%) as a result of noise from the large spectral variability of surface reflectance from some land surface types. POFD values for dust detection over nonbright surface are much lower (27%). Future work will involve the use of NDVI to flag bright surfaces with no dust over them, so the surface is not falsely identified as airborne dust. In addition, DAI comparisons dust detection of DAI-based algorithm with AERONET measurements show accuracy, POCD, and POFD are 70%, 67%, and 23%, respectively. The accuracy and POCD values are slightly lower because of limited matchups available between detection from DAI-based algorithm and AERONET near the source regions where most of the dust plumes are observed. However, the AERONET stations close to the source region or stations located at coast or island showed accuracy and POCD values close to 80% and 85%, respectively.

Like all the algorithms based on a universal threshold, the advantages of DAI are that it is simple, fast, and very suitable for generating operational product globally in real time. However, the use of a single threshold value can also lead to misclassification if the threshold value becomes sensitive to changing sensor characteristics, viewing and illuminating geometry, surface type, and composition of dust. The latter two have been investigated and found to be not of significance, but future work will focus on the development of a Normalized Difference Vegetation Index (NDVI)-based threshold for DAI. The insensitivity of DAI to thin dust layer (AODs <0.2) is due to the selection of threshold, which maximizes true detections and minimizes false positives. If the threshold is relaxed, thin dust layers can be picked up, but this will also increase the POFD; POFD values are also high over sunglint regions. However, DAI is not computed for sunglint regions that can be identified by illuminating and viewing geometry. Similar to glint values over ocean, bright surfaces when atmosphere is clear can also lead to high POFD values due to which DAI is not computed when pixels are identified to be bright based on NDVI. As for the changing viewing and illuminating geometry, it is found that the threshold is less sensitive for sunglint-free ocean surface but becomes more sensitive for thin dust over land surface. Especially, it becomes difficult to detect thin dust over land surface for the combination of a lower SZA with a lower VZA.

Unlike other dust detection techniques that depend largely on measurements at thermal infrared wavelengths, this algorithm uses measurements made in the deep blue and blue part of the visible spectrum and shortwave IR. It provides a dust detection capability, over both land and water, except for over sunglint region. Comparisons with DA method [*Cho et al.*, 2013] and MCI algorithm [*Zhao et al.*, 2010] against CALIOP VFM indicate that DAI-based dust identification algorithm has also a comparable performance with DA method over ocean, but much better performance than MCI algorithm over both land and ocean due to the fact that MCI algorithm is optimized for thick dust plumes, while the CALIOP VFM matchups are dominated by thinner and intermediate dust layers or plumes. Compared with AERONET observation over coastal stations, DAI-based dust identification algorithm has also a comparable performance with DA methods. However, DAI-based dust identification algorithm has advantage over DA method in detecting thick dust plumes and separating other absorbing aerosols, such as smoke, from dust, while DA method may perform better for detecting thin dust since it is specifically designed and optimized for detecting thin dust.

The algorithm was developed for MODIS observations, but it is applicable to the observations from Suomi National Polar Partnership (NPP) Visible Infrared Imaging Radiometer Suite (VIIRS). This will continue the MODIS legacy and extend the dust detection to the next generation satellite sensors.

The dust detection product can be used in the quantitative retrieval of aerosol optical thickness by forcing the algorithm to select a lookup table generated for a dust aerosol model. For air quality related applications, the product is useful to evaluate dust forecasts, monitor and document dust outbreaks, and contribute to the improvements of air quality models.

Acknowledgments
Authors like to thank Hongqing Liu, Istvan Laszlo, and Jian Zeng for valuable and constructive discussions during the development of the algorithm. Authors also would like to thank reviewers for valuable comments and suggestions which helped us improve the paper. Authors extend their gratitude to PIs of NASA AERONET, MODIS, and CALIPSO projects for providing the data.

References

Ackerman, S. A. (1989), Using the radiative temperature difference at 3, 7 and 11 um to track dust outbreaks, *Remote Sens. Environ.*, *27*, 129–133.

Ackerman, S. A. (1997), Remote sensing aerosols using satellite infrared observations, *J. Geophys. Res.*, *102*, 17,069–17,079.

Al-Saadi, J., et al. (2005), Improving national air quality forecasts with weather satellite aerosol observations, *Bull. Am. Meteorol. Soc.*, *86*, 1249–1261.

Ashpole, I., and R. Washington (2012), An automated dust detection using SEVIRI: A multiyear climatology of summertime dustiness in the central and western Sahara, *J. Geophys. Res.*, *117*, D08202, doi:10.1029/2011JD016845.

Bullard, J. E., M. C. Baddock, G. H. McTainsh, and J. F. Leys (2008), Sub-basin scale dust source geomorphology detected using MODIS, *Geophys. Res. Lett.*, *35*, L15404, doi:10.1029/2008GL033928.

Burton, S. P., R. A. Ferrare, M. A. Vaughan, A. H. Omar, R. R. Rogers, C. A. Hostetler, and J. W. Hair (2013), Aerosol classification from airborne HSRL and comparisons with the CALIPSO vertical feature mask, *Atmos. Meas. Tech. Discuss.*, *6*(1), 1815–1858.

Cho, H.-M., S. L. Nasiri, P. Yang, I. Laszlo, and X. Zhao (2013), Detection of optically thin mineral dust aerosol layers over the ocean using MODIS, *J. Atmos. Oceanic Technol.*, *30*, 896–916.

Darmenov, A., and I. N. Sokolik (2005), Identifying the regional thermal-IR radiative signature of mineral dust with MODIS, *Geophys. Res. Lett.*, *32*, L16803, doi:10.1029/2005GL023092.

Darmenov, A., and I. N. Sokolik (2009), Spatial variability of satellite visible radiances in dust and dust-cloud mixed conditions: Implications for dust detection, *Geophys. Res. Lett.*, *36*, L14811, doi:10.1029/2009GL038383.

Dubovik, O., B. Holben, T. F. Eck, A. Smirnov, Kaufman, Y. J., King, M. D., D. Tanre, and I. Slutsker (2002), Variability of absorption and optical properties of key aerosol types observed in worldwide locations, *J. Atmos. Sci.*, *59*, 590—608.

Dubovik, O., B. N. Holben, T. Lapyonok, A. Sinyuk, M. I. Mishchenko, P. Yang, and I. Slutsker (2006), Application of light scattering by spheroids for accounting for particle nonsphericity in remote sensing of desert dust, *J. Geophys. Res.*, *111*, D11208, doi:10.1029/2005JD006619.

Eck, T. F., B. N. Holben, J. S. Reid, O. Dubovik, A. Smirnov, N. T. O'Neill, I. Slutsker, and S. Kinne (1999), Wavelength dependence of the optical depth of biomass burning, urban, and desert dust aerosols, *J. Geophys. Res.*, *104*(D24), 31,333–31,349, doi:10.1029/1999JD900923.

Evan, A. T., A. K. Heidinger, and M. J. Pavolonis (2006), Development of a new over-water advanced very high resolution radiometer dust detection algorithm, *Int. J. Remote Sens.*, *27*, 3903–3924, doi:10.1080/01431160600646359.

Hansell R. A., S. C. Ou, K. N. Liou, J. K. Roskovensky, S. C. Tsay, C. Hsu, and Q. Ji (2007), Simultaneous detection/separation of mineral dust and cirrus clouds using MODIS thermal infrared window data, *Geophys. Res. Lett.*, *34*, L13802, doi:10.1029/2007GL031035.

Herman, J. R., P. K. Bhartia, O. Torres, N. C. Hsu, C. J. Seftor, and E. Celarier (1997), Global distribution of UV-absorbing aerosols from Nimbus 7/TOMS data, *J. Geophys. Res.*, *102*(D14), 16,911–16,921.

Holben, B. N. (1998), AERONET—A federated instrument network and data archive for aerosol characterization, *Remote Sens. Environ.*, *66*, 1–16.

Holben, B. N., et al. (2001), An emerging ground-based aerosol climatology: Aerosol optical depth from AERONET, *J. Geophys. Res.*, *106*(D11), 12,067–12,097, doi:10.1029/2001JD900014.

Hsu, N. C., J. R. Herman, O. Torres, B. N. Holben, D. Tanre, T. F. Eck, A. Smirnov, B. Chatenet, and F. Lavenu (1999), Comparisons of the TOMS aerosol index with Sun-photometer aerosol optical thickness: Results and applications, *J. Geophys. Res.*, *104*(D6), 6269–6279, doi:10.1029/1998JD200086.

Hsu, N. C., W. D. Robinson, S. W. Bailey, and P. J. Werdell (2000), The description of the SeaWiFS absorbing aerosol index *SeaWiFS*, *NASA Tech. Memorandum*, *2000-206892*(10), 3–5.

Hsu, N. C., S.-C. Tsay, M. D. King, and J. R. Herman (2004), Aerosol properties over bright reflecting source regions, *IEEE Trans. Geosci. Remote Sens.*, *42*(3), 557–569, doi:10.1109/TGRS.2004.824067.

Hsu, N. C., S.-C. Tsay, M. D. King, and J. R. Herman (2006), Deep blue retrievals of Asian aerosol properties during ACE-Asia, *IEEE Trans. Geosci. Remote Sens.*, *44*(11), 3180–3195, doi:10.1109/TGRS.2006.879540.

Hu, X. Q., N. M. Lu, T. Niu, and P. Zhang (2008), Operational retrieval of Asian sand and dust storm from FY-2C geostationary meteorological satellite and its application to real time forecast in Asia, *Atmos. Chem. Phys.*, *8*, 1649–1659.

Intergovernmental Panel on Climate Change (2007), Climate change 2007: The physical science basis, in *Contribution of Working Group I to the Fourth Assessment Report of the Intergovernmental Panel on Climate Change*, edited by S. Solomon et al., 996 pp., Cambridge Univ. Press, Cambridge, U. K., and New York.

Jankowiak, I., and D. Tanré (1992), Satellite climatology of Saharan dust outbreaks: Method and preliminary results, *J. Clim.*, *5*, 646–656.

Kaufman, Y. J., D. Tanré, L. Remer, E. Vermote, A. Chu, and B. N. Holben (1997), Remote sensing of tropospheric aerosol from EOS-MODIS over the land using dark targets and dynamic aerosol models, *J. Geophys. Res.*, *102*(D14), 17,051–17,067.

Kaufman, Y. J., A. Karnieli, and D. Tanré (2000), Detection of dust over deserts using satellite data in the solar wavelengths, *IEEE Geosci. Remote Sens.*, *38*(1), 525–531.

Kim, K. M., W. K.-M. Lau, Y. C. Sud, and G. K. Walker (2010), Influence of aerosol-radiative forcing on the diurnal and seasonal cycles of rainfall over West Africa and Eastern Atlantic Ocean using GCM simulations, *Clim. Dyn.*, *26*, doi:10.1007/s00382-010-0750-1.

Klüser, L., and K. Schepanski (2009), Remote sensing of mineral dust over land with MSG infrared channels: A new bitemporal mineral dust index, *Remote Sens. Environ.*, *113*, 1853–1867, doi:10.1016/j.rse.2009.04.012.

Kotchenova, S. Y., E. F. Vermote, R. Matarrese, and F. J. Klemm Jr. (2006), Validation of a vector version of the 6S radiative transfer code for atmospheric correction of satellite data, *Part I. Path Radiance, Appl. Opt.*, *45*(26), 6726–6774.

Kwiatkowska, E. J., B. A. Franz, G. Meister, C. R. McClain, and X. Xiong (2008), Cross calibration of ocean-color bands from Moderate Resolution Imaging Spectroradiometer on Terra platform, *Appl. Opt.*, *47*(36), 6796–6810.

Legrand, M., A. Plana-Fattori, and C. N'doume (2001), Satellite detection of dust using the IR imagery of Meteosat: 1. Infrared differences dust index, *J. Geophys. Res.*, *106*(D16), 18,251–18,274.

Li, R. R., L. Remer, Y. J. Kaufman, S. Mattoo, B. C. Gao, and E. Vermote (2005), Snow and ice mask for the MODIS aerosol products, *IEEE Geosci. Remote Sens. Lett.*, *2*(3), 306–310.

Liu, Z., et al. (2008), CALIPSO lidar observations of the optical properties of Saharan dust: A case study of long-range transport, *J. Geophys. Res.*, *113*, D07207, doi:10.1029/2007JD008878.

Liu, Z., M. A. Vaughan, D. M. Winker, C. Kittaka, R. E. Kuehn, B. J. Getzewich, C. R. Trepte, and C. A. Hostetler (2009), The CALIPSO lidar cloud and aerosol discrimination: Version 2 algorithm and initial assessment of performance, *J. Atmos. Oceanic Technol.*, *26*, 1198–1213.

Martins, J. V., D. Tanré, L. Remer, Y. Kaufman, S. Mattoo, and R. Levy (2002), MODIS Cloud screening for remote sensing of aerosol over oceans using spatial variability, *Geophys. Res. Lett.*, *29*(12), 1619, doi:10.1029/2001GL013252.

Mielonen, T., A. Arola, M. Komppula, J. Kukkonen, J. Koskinen, G. de Leeuw, and K. E. J. Lehtinen (2009), Comparison of CALIOP level 2 aerosol subtypes to aerosol types derived from AERONET inversion data, *Geophys. Res. Lett.*, *36*, L18804, doi:10.1029/2009GL039609.

Miller, S. D. (2003), A consolidated technique for enhancing desert dust storms with MODIS, *Geophys. Res. Lett.*, *30*(20), 2071, doi:10.1029/2003GL018279.

Nicholson, S. E. (2000), Land surface processes and Sahel climate, *Rev. Geophys.*, *38*(1), 117–139.

Prospero, J. M., and P. J. Lamb (2003), African droughts and dust transport to the Caribbean: Climate change implications, *Science*, *302*, 1024–1027.

Ramirez-Beltran, N. D., R. Kuligowski and E. Harmsen (2008), Validation and strategies to improve the hydro-estimator and NEXRAD over Puerto Rico, paper presented at 12th WSEAS International Conference on SYSTEMS, Heraklion, Greece, 22–24 July.

Remer, L. A., D. Tanre, Y. J. Kaufman, R. Levy and S. Mattoo (2006), Algorithm for remote sensing of tropospheric aerosol from MODIS: Collection 5, Product ID MOD04/MYD04.

Schepanski, K., I. Tegen, B. Laurent, B. Heinold, and A. Macke (2007), A new Saharan dust source activation frequency map derived from MSG–SEVIRI IR-channels, *Geophys. Res. Lett.*, *34*, L18803, doi:10.1029/2007GL030168.

Shi, W., and M. Wang (2007), Detection of turbid waters and absorbing aerosols for the MODIS ocean color data processing, *Remote Sens. Environ.*, *110*, 149–161.

Smirnov, A., B. N. Holben, T. F. Eck, O. Dubovik, and I. Slutsker (2000), Cloud-screening and quality control algorithms for the AERONET database, *Remote Sens. Environ.*, *73*(3), 337–349.

Sokolik, I. N. (2002), The spectral radiative signature of wind-blown mineral dust: Implications for remote sensing in the thermal IR region, *Geophys. Res. Lett.*, *29*(24), 2154, doi:10.1029/2002GL015910.

Tan, S.-C., G.-Y. Shi, J.-H. Shi, H.-W. Gao, and X. Yao (2011), Correlation of Asian dust with chlorophyll and primary productivity in the coastal seas of China during the period from 1998 to 2008, *J. Geophys. Res.*, *116*, G02029, doi:10.1029/2010JG001456.

Torres, O., P. K. Bhartia, J. R. Herman, and A. Sinyuk (2002), Aerosol properties from EP-TOMS near UV observations, *Adv. Space Res.*, *29*, 1771–1780.

Vaughan, M., K. A. Powell, D. M. Winker, C. A. Hostetler W. H. Hunt, B. J. Getzewich, S. A. Young, Z. Liu, and M. J. McGill (2009), Fully automated detection of cloud and aerosol layers in the CALIPSO lidar measurements, *J. Atmos. Oceanic Technol.*, *26*, 2034–2050.

Wilks, D. S. (1995), *Statistical Methods in the Atmospheric Sciences: An Introduction*, 467 pp., Acad. Press, San Diego, Calif.

Winker, D. M., M. A. Vaughan, A. Omar, Y. X. Hu, K. A. Powell, Z. Y. Liu, W. H. Hunt, and S. A. Young (2009), Overview of the CALIPSO mission and CALIOP data processing algorithms, *J. Atmos. Oceanic Technol.*, *26*, 2310–2323, doi:10.1175/2009JTECHA1281.1.

Winker, D. M., et al. (2010), The CALIPSO mission: A global 3D view of aerosols and clouds, *Bull. Am. Meteorol. Soc.*, *91*, 1211–1229, doi:10.1175/2010BAMS3009.

Xie, Y. (2009), Detection of smoke and dust aerosols using multi-sensor satellite remote sensing measurements, PhD dissertation, Georgia Mason Univ.

Yoshioka, M., and N. M. Mahowald (2007), Impact of desert dust radiative forcing on Sahel precipitation: Relative importance of dust compared to sea surface temperature variations, vegetation changes, and greenhouse gas warming, *J. Clim.*, *20*, 1445–1467.

Zhao, C., X. Liu, L. Ruby Leung, and S. Hagos (2011), Radiative impact of mineral dust on monsoon precipitation variability over West Africa, *Atmos. Chem. Phys.*, *11*, 1879–1893, doi:10.5194/acp-11-1879-2011.

Zhao, T. X.-P., S. Ackerman, and W. Guo (2010), Dust and smoke detection for multi-channel imagers, *Remote Sens.*, *2*, 2347–2368, doi:10.3390/rs2102347.